JGR Atmospheres

RESEARCH ARTICLE
10.1029/2023JD039518

Measurements and Modeling of the Interhemispheric Differences of Atmospheric Chlorinated Very Short-Lived Substances

Behrooz Roozitalab[1], Louisa K. Emmons[1], Rebecca S. Hornbrook[1], Douglas E. Kinnison[1], Rafael P. Fernandez[2], Qinyi Li[2,3,4], Alfonso Saiz-Lopez[2], Ryan Hossaini[5], Carlos A. Cuevas[2], Alan J. Hills[1], Stephen A. Montzka[6], Donald R. Blake[7], William H. Brune[8], Patrick R. Veres[9], and Eric C. Apel[1]

[1]Atmospheric Chemistry Observations & Modeling Laboratory, NSF National Center for Atmospheric Research, Boulder, CO, USA, [2]Department of Atmospheric Chemistry and Climate, Institute of Physical Chemistry Blas Cabrera, CSIC, Madrid, Spain, [3]Department of Civil and Environmental Engineering, The Hong Kong Polytechnic University, Hong Kong, China, [4]Now at Environment Research Institute, Shandong University, Qingdao, China, [5]Lancaster Environment Centre, Lancaster University, Lancaster, UK, [6]Global Monitoring Laboratory, National Oceanic and Atmospheric Administration, Boulder, CO, USA, [7]Department of Chemistry, University of California, Irvine, CA, USA, [8]Department of Meteorology and Atmospheric Science, Pennsylvania State University, University Park, PA, USA, [9]Research Aviation Facility, Earth Observing Laboratory, NSF National Center for Atmospheric Research, Boulder, CO, USA

Key Points:

- Coincident global scale airborne data from multiple instruments of chlorinated very short-lived substances (Cl-VSLS) provide insights into their distributions and inter-comparability of measurements
- The updated model reasonably simulates the global distribution of the major Cl-VSLS species and their relative contributions to the tropospheric chlorine burden
- Model results show a disproportionately high impact of Asian Cl-VSLS emissions regionally and globally throughout the troposphere

Supporting Information:

Supporting Information may be found in the online version of this article.

Correspondence to:

B. Roozitalab and E. C. Apel,
behroozr@ucar.edu;
apel@ucar.edu

Citation:

Roozitalab, B., Emmons, L. K., Hornbrook, R. S., Kinnison, D. E., Fernandez, R. P., Li, Q., et al. (2024). Measurements and modeling of the interhemispheric differences of atmospheric chlorinated very short-lived substances. *Journal of Geophysical Research: Atmospheres*, *129*, e2023JD039518. https://doi.org/10.1029/2023JD039518

Received 23 JUN 2023
Accepted 6 JAN 2024

Abstract Chlorinated very short-lived substances (Cl-VSLS) are ubiquitous in the troposphere and can contribute to the stratospheric chlorine budget. In this study, we present measurements of atmospheric dichloromethane (CH_2Cl_2), tetrachloroethene (C_2Cl_4), chloroform ($CHCl_3$), and 1,2-dichloroethane (1,2-DCA) obtained during the National Aeronautics and Space Administration (NASA) Atmospheric Tomography (ATom) global-scale aircraft mission (2016–2018), and use the Community Earth System Model (CESM) updated with recent chlorine chemistry to further investigate their global tropospheric distribution. The measured global average Cl-VSLS mixing ratios, from 0.2 to 13 km altitude, were 46.6 ppt (CH_2Cl_2), 9.6 ppt ($CHCl_3$), 7.8 ppt (1,2-DCA), and 0.84 ppt (C_2Cl_4) measured by the NSF NCAR Trace Organic Analyzer (TOGA) during ATom. Both measurements and model show distinct hemispheric gradients with the mean measured Northern to Southern Hemisphere (NH/SH) ratio of 2 or greater for all four Cl-VSLS. In addition, the TOGA profiles over the NH mid-latitudes showed general enhancements in the Pacific basin compared to the Atlantic basin, with up to ∼18 ppt difference for CH_2Cl_2 in the mid troposphere. We tagged regional source emissions of CH_2Cl_2 and C_2Cl_4 in the model and found that Asian emissions dominate the global distributions of these species both at the surface (950 hPa) and at high altitudes (150 hPa). Overall, our results confirm relatively high mixing ratios of Cl-VSLS in the UTLS region and show that the CESM model does a reasonable job of simulating their global abundance but we also note the uncertainties with Cl-VSLS emissions and active chlorine sources in the model. These findings will be used to validate future emission inventories and to investigate the fast convective transport of Cl-VSLS to the UTLS region and their impact on stratospheric ozone.

Plain Language Summary The Montreal Protocol has phased down the consumption and production of a large number of halogenated compounds such as CFCs, due to their potential for depleting stratospheric ozone. However, the consumption and production of a class of halogenated compounds, referred to as very short-lived substances (VSLS), is not controlled by the Montreal Protocol. Evidence is growing that globally increasing emissions of human-produced chlorinated VSLS (Cl-VSLS) could have an impact on stratospheric ozone. In this work, we present comprehensive aircraft measurements coupled to modeling of the major speciated Cl-VSLS that show their present day global distribution at altitudes up to 12 km and also show that Asian emissions are responsible for the majority of observed Cl-VSLS throughout the troposphere including the Southern Hemisphere.

1. Introduction

Very short-lived substances (VSLS) include the class of halogen (Cl, Br, and I) containing substances that have atmospheric lifetimes typically less than 6 months. While the majority of VSLS emissions are photochemically

destroyed in the troposphere during their lifetime, the *Scientific Assessment of Ozone Depletion* reports—as early as the 1998 edition—have shown that these species do enter the stratosphere and affect the stratospheric ozone layer, with the latest findings reported in the 2022 edition (hereafter called SAOD-2022) by Laube et al. (2022). Unlike brominated VSLS (Br-VSLS) which are primarily emitted by natural sources (Carpenter & Liss, 2000; Keng et al., 2021), chlorinated VSLS (Cl-VSLS) have significant anthropogenic sources (Claxton et al., 2020; Keene et al., 1999) and their relative importance is increasing as their estimated contribution to the total stratospheric chlorine abundance has increased from ∼2% in 2000 to ∼3.4% in 2017 (Hossaini et al., 2019). This increase is attributed to both reduction of long-lived chlorocarbons and growth of Cl-VSLS abundance (Hossaini et al., 2019). Specifically, the sum of total chlorine from VSLS in the stratosphere (through source gas injection + product gas injection) has increased from 80 parts per trillion (ppt) in 1993 to 130 ppt in 2020 (Laube et al., 2022). In addition, although chlorine is reported to be 45–74 times less efficient than bromine in destroying ozone based on several modeling studies (Daniel et al., 1999; Klobas et al., 2020; Sinnhuber et al., 2009), Cl-VSLS could be as important as Br-VSLS due to their high mixing ratios. For example, Oram et al. (2017) observed high Cl-VSLS mixing ratios at the surface over eastern Asia (median of 755.8 ppt of chlorine in Taiwan) which are about 116 times higher than reported Br-VSLS in the SAOD-2022 (Laube et al., 2022). Oram et al. (2017) also reported high concentrations of Cl-VSLS in tropical regions over the western Pacific Ocean, where they can be rapidly uplifted to the upper troposphere. Additionally, it is shown that keeping the Cl-VSLS flux constant (compared to a zero Cl-VSLS flux scenario) will delay the return date of total column ozone to 1980 levels by approximately seven years (Chipperfield et al., 2020; Dhomse et al., 2019; Laube et al., 2022). Long-lived chlorinated ozone depleting substances (ODSs; i.e., CFCs, HCFCs, etc.) have been overall successfully controlled under the Montreal Protocol. Hence, a better understanding of the sources, global abundance, distribution, and transport of Cl-VSLS to the stratosphere has become more crucial to ensure that their trends do not slow down the progress made in reducing atmospheric Cl and Br abundance and significant progress has been made in addressing this issue (Adcock et al., 2021; An et al., 2021; Claxton et al., 2020; Feng et al., 2018; Hossaini et al., 2019; Keng et al., 2021; Lauther et al., 2022; Pan et al., 2017; Thompson et al., 2022).

The most abundant Cl-VSLS in the atmosphere are dichloromethane (CH_2Cl_2), chloroform ($CHCl_3$), 1,2-dichloroethane (CH_2ClCH_2Cl, herein referred to as 1,2-DCA) and tetrachloroethene (C_2Cl_4). The atmospheric lifetimes of these Cl-VSLS differ regionally with the longest lifetimes at high latitudes and altitudes. The SAOD-2022 reported both an average (and a range) for their lifetimes: 1,2-DCA = 81.3 days (41–555 days) and C_2Cl_4 = 109 days (66–245 days), $CHCl_3$ = 178 days (97–1145 days), and CH_2Cl_2 = 176 days (95–1070 days). $CHCl_3$, has significant emissions by natural sources (Feng et al., 2018; Worton et al., 2006), but the other three atmospherically abundant Cl-VSLS compounds are largely (about 90%) anthropogenic (Laube et al., 2022) and primarily used in industry. $CHCl_3$ also has industrial sources and is used in chemical manufacturing; its global emission trend between 2010 and 2015 is explained entirely by increasing emissions in eastern Asia (Fang et al., 2019). Nevertheless, long-term ground observations by the Advanced Global Atmospheric Gases Experiment (AGAGE) network suggest $CHCl_3$ is currently stable; its annual mean mole fraction remained constant at 8.7 ppt in 2019 and 2020 (Laube et al., 2022).

CH_2Cl_2 is a co-product of industrial production of $CHCl_3$ and is used as a versatile chemical solvent and degreasing agent (Feng et al., 2018). It had global annual mean mole fractions of 38.3 and 45.5 ppt in 2020 based on the AGAGE and National Oceanic and Atmospheric Administration (NOAA) networks, respectively (Laube et al., 2022). Asia is currently recognized to be the main source region of CH_2Cl_2 with the largest contributions from China and India (An et al., 2021; Feng et al., 2018; Say et al., 2019). It has been estimated that Asian emissions of CH_2Cl_2 increased annually by 51 Gg yr^{-1} from 2006 to 2017 (Claxton et al., 2020). Sustained growth in the atmospheric CH_2Cl_2 mole fraction in coming decades could delay the recovery of stratospheric ozone over Antarctica (Hossaini et al., 2017). However, the rate of increase of global abundance of CH_2Cl_2 slowed after 2016, potentially due to regulatory control and economic drivers (An et al., 2021; Laube et al., 2022).

C_2Cl_4, with annual global mole fractions in the low ppt range, is used as both a dry cleaning solvent and industrial precursor (Laube et al., 2022; Simpson et al., 2004). Unlike CH_2Cl_2, emissions of C_2Cl_4 are of the same order in Asia, North America, and Europe (Claxton et al., 2020). While C_2Cl_4, with four Cl atoms, has the largest number of Cl atoms per molecule amongst the Cl-VSLS discussed, it has a shorter lifetime than CH_2Cl_2 and the emissions of this toxic compound have declined in recent years owing to controls in different countries on its use (Claxton et al., 2020). Similarly, 1,2-DCA which is most commonly used in the production of vinyl chloride (chloroethene), is also a toxic compound. Although not much is known about its global budget as it is not reported by long-term observations networks, limited observations suggest it is the second most abundant

Cl-VSLS after CH_2Cl_2 and in some regions of the atmosphere it has a very large abundance (Laube et al., 2022; Oram et al., 2017). Oram et al. (2017) reported 1,2-DCA ground-level mole fractions up to 309 ppt in Taiwan and estimated its annual Asian emissions at about 203 Gg, based on CH_2Cl_2 emissions and its positive correlation with 1,2-DCA measurements.

Due to their non-uniform emissions and relatively short lifetimes, Cl-VSLS have large variability in their global tropospheric distribution (zonally, meridionally, and vertically), with higher mole fractions close to their source regions. CH_2Cl_2 ground measurements show up to 3.5 times higher mole fractions in the Northern Hemisphere (NH) than in the Southern Hemisphere (SH) (Laube et al., 2022). Additionally, a large vertical gradient is reported over the tropics with sharper slopes for shorter-lived VSLS species (e.g., C_2Cl_4) (Andrews et al., 2016; Pan et al., 2017). Also, there is a significant difference between the global CH_2Cl_2 mean mole fractions reported by AGAGE and NOAA networks, only some of which could be explained by calibration differences, suggesting an impact due to differing sampling locations (Laube et al., 2022). Since the measurements by global networks are also used for developing top-down emission estimates, the limited spatial coverage of measurement stations leads to differences between top-down and bottom-up inventories (An et al., 2021). Similarly, most airborne campaigns that measured VSLS within the last decade focused on specific regions or times of the year (Adcock et al., 2021; Jesswein et al., 2022; Keber et al., 2020; Leedham Elvidge et al., 2015; Oelhaf et al., 2019). In particular, the CAST (Coordinated Airborne Studies in the Tropics), CONTRAST (CONvective TRansport of Active Species in the Tropics), and ATTREX (Airborne Tropical TRopopause EXperiment) airborne studies measured Cl-VSLS over the tropical western Pacific Ocean during January and February 2014 (Andrews et al., 2016; Harris et al., 2017; Pan et al., 2017). Additionally, the ORCAS (O_2/N_2 Ratio and CO_2 Airborne Southern Ocean Study) airborne study (January–February 2016) measured Cl-VSLS over the Southern Ocean (Stephens et al., 2018). In contrast, this study is focused on measurements made during the NASA Atmospheric Tomography (ATom) mission (Thompson et al., 2022), a recent global-scale multi-year mission (2016–2018), which included observations of Cl-VSLS from the NCAR Trace Organic Gas Analyzer (TOGA), the University of California, Irvine Whole Air Sampler (UCI WAS), and the NOAA Programmable Flask Package (PFP) instruments, throughout all four seasons, to characterize their global chemistry and transport.

Halogens have a broad range of impacts on atmospheric chemistry, including catalytic loss of tropospheric ozone. In particular, rapid cycling between halogen radicals and their reservoirs converts NO_x to HNO_3, reducing ozone concentrations, which further affects the OH abundance as the principal atmospheric oxidant (Li et al., 2022; Simpson et al., 2015; Wang et al., 2021). The recent addition of halogen chemistry to global models has enabled scientists to better understand the global impact of chlorine sources on atmospheric chemistry (Fernandez et al., 2014; Ordóñez et al., 2012; Saiz-Lopez and von Glasow, 2012; Simpson et al., 2015; Wang et al., 2021). Hossaini et al. (2016) updated the tropospheric chlorine chemistry in the TOMCAT model, which was used later by Claxton et al. (2020) to constrain the global emissions of CH_2Cl_2 and C_2Cl_4 based on available atmospheric long-term and campaign-based measurements. Hossaini et al. (2019), Chipperfield et al. (2018), and Chipperfield et al. (2020) used this updated TOMCAT model to investigate the trend of stratospheric chlorine from Cl-VSLS, their impact on lower stratospheric ozone, and ozone layer recovery, respectively. Li et al. (2022) updated the halogen chemistry in the Community Earth System Model (CESM) and studied the impact of halogens on the global methane burden. Nevertheless, prior to this study a comprehensive evaluation of the global models in reproducing the global distribution and seasonal variation of Cl-VSLS had not been performed.

In this work, we present the spatial and vertical distribution of CH_2Cl_2, C_2Cl_4, 1,2-DCA, and $CHCl_3$ measured by the TOGA, WAS, and PFP instruments during ATom. We highlight the latitudinal and seasonal variability of Cl-VSLS and use tracers to understand their distributions and interhemispheric difference. The CESM model with updated chlorine chemistry is used to simulate the Cl-VSLS during the ATom mission period and the model output is compared with the measurements. We also evaluate the model results against co-located AGAGE and NOAA ground-site observations and use the reaction rate information from the model output to investigate the dominant photochemical destruction pathways of Cl-VSLS. Finally, we tag the emissions in different regions of the world to estimate their impact on global tropospheric abundance of Cl-VSLS.

2. Methods

2.1. Measurements

This work is primarily based on observations made during the NASA ATom mission. ATom was a global-scale mission that flew the heavily instrumented NASA DC-8 aircraft over remote regions during four seasons between

Table 1
Summary of Airborne Missions and Measurement Instruments Used in This Study

Instrument	Mission (# of samples)	Methodology	Measurement details	Inlet setup	Reported uncertainties[a] CH_2Cl_2	C_2Cl_4	$CHCl_3$	1,2-DCA	Ref.
NCAR TOGA	ATom (12,168), ORCAS (2,573), CONTRAST (3,568)	in situ Fast GC/MS	35-s samples every 2 min	Heated Sulfinert® tubing	±15%	±30%	±15%	±30%	Apel et al. (2015)
UCI WAS	ATom (6,991)	Stainless steel flask collection and laboratory analysis by multi-detector GC	Variable—flasks sampled on demand (average 45-s sample every 3.5 min)	Unheated stainless steel	±20%	±20%	±20%	±25%	Simpson et al. (2010)
NOAA PFP	ATom (1,121)	Glass flask collection and laboratory analysis by GC/MS	Variable—flasks sampled on demand (average 15-s sample every 10–20 min)	Chemically passivated SS tubing	±10%	±15%	±20%	±15%	Sweeney et al. (2015); Hu et al. (2015)

[a]The uncertainties reported here represent the combination of estimated scale uncertainties and measurement precision.

2016 and 2018 (Thompson et al., 2022). Specifically, ATom collected measurements, with regular profiling between 200 m and ~13 km altitude, from 28 July to 22 August 2016 (ATom-1), 26 January to 22 February 2017 (ATom-2), 28 September to 26 October 2017 (ATom-3), and 24 April to 21 May 2018 (ATom-4). In this work, we assign each ATom deployment to the month with the majority of data, for example, August 2016 for ATom-1. This mission provides a comprehensive data set to characterize the chemistry and transport of chemical species in the remote regions of the troposphere and the UTLS (upper troposphere and lower stratosphere). We specifically present the Cl-VSLS data measured during the ATom mission. In addition, we compare ATom data with our TOGA measurements made during ORCAS and CONTRAST and use surface observation data measured by ground monitoring networks around the globe to complement the evaluation of the model performance.

Table 1 summarizes the measurements used in this study.

2.1.1. ATom Cl-VSLS Observations

As shown in Figure 1, the ATom mission consisted of four deployments with very similar near-pole-to-pole flight tracks over remote regions with regular profiling throughout much of the troposphere, which provides a unique data set to better understand the spatial and seasonal variations of Cl-VSLS. Within these deployments, three systems provided measurements of Cl-VSLS mixing ratios: (a) the NCAR Trace Organic Gas Analyzer (TOGA) instrument, (b) the University of California, Irvine Whole Air Sampler (UCI WAS), and (c) the NOAA Programmable Flask Package (PFP).

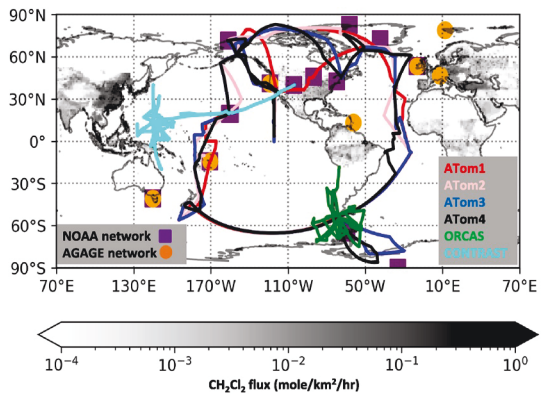

Figure 1. Map of the flight tracks for individual ATom deployments, and ORCAS and CONTRAST missions. The ground measurement sites in the NOAA and AGAGE networks used in this study are also shown. The map is shaded by the 2016 annual average CH_2Cl_2 emissions developed by Claxton et al. (2020).

The three systems used in this study to measure Cl-VSLS, have been previously documented in the literature and will only be briefly described here. TOGA is an in situ fast gas chromatograph quadrupole mass spectrometer (GC/MS) that continuously measures a wide range of VOCs. During ATom, TOGA analyzed samples collected over 35 s every 2 min (Apel et al., 2015). The UCI WAS (Simpson et al., 2010) had 168 electropolished stainless steel (SS) canisters on board for each flight and collected pressurized whole air samples throughout the flights, sampling every 2–5 min for between 20 s and 2 min in duration, pressure altitude dependent. Post flight, the canisters were returned to the UCI laboratory where they were analyzed using a series of gas chromatographs. Likewise, the NOAA PFP (Hu et al., 2015; Sweeney et al., 2015) system collected whole air samples in up to 24 glass flasks per flight (48 flasks during ATom-2), typically averaging one 10-s to 20-s sample every 10–20 min. These flasks were returned to the NOAA laboratory for

analysis by gas chromatography with mass spectrometric detection. Data obtained from all three methodologies were used to analyze results for a large suite of VOCs, including Cl-VSLS. TOGA uses NOAA calibration scales and on-board standards and cross calibrates with a multi-component calibration standard from the National Institute of Standards and Technology (NIST). Specifically, TOGA referenced their measurements for CH_2Cl_2 and $CHCl_3$ to the NOAA ESX-3583 standard and referenced their measurements for C_2Cl_4 and 1,2-DCA to the NIST CAL 014921 calibration mixture, respectively. In addition, TOGA used NCAR prepared standards as in-flight working standards for all species. NOAA PFP used their calibration scales for all the compounds including a recently developed NOAA-2019 scale for 1,2-DCA. UCI-WAS data are reported based on their own set of calibration standards and thus their calibration is independent of both NOAA PFP and NCAR TOGA.

The TOGA instrument measured 12,168 samples during the four ATom deployments, and WAS and PFP collected and analyzed 6,991 and 1,109 flask samples, respectively. For statistical analyses of the data, we replaced observations below the lower limit of detection (LLOD) with 0.5 × LLOD based on the U.S. EPA guidance for data quality assessment (USEPA, 2000); approximately 15% of TOGA samples were below the LLOD for C_2Cl_4 (Table S1 in Supporting Information S1). For comparisons to the observations, the model output was sampled instantaneously along the ATom flight tracks using TOGA sampling times and locations. We use normalized mean bias (NMB), root mean squared error (RMSE), and Pearson correlation coefficient (r) as statistical metrics for evaluation.

2.1.2. Ground-Based Observations

We used the monthly mean mole fractions of ground-based CH_2Cl_2 and C_2Cl_4 measurements for a 3-year period, 2016–2018, from the National Oceanic and Atmospheric Administration (NOAA) and Advanced Global Atmospheric Gases Experiment (AGAGE) monitoring networks (Claxton et al., 2020; Prinn et al., 2018). Specifically, we used data from 14 NOAA and 7 AGAGE sites measured using GC/MS systems (the stations used are listed in Table S2 in Supporting Information S1). As shown in Figure 1, the majority of these sites are located in the NH, and co-located measurements are made by these networks at four sites (two in each hemisphere). For CH_2Cl_2, the NOAA and AGAGE networks use NOAA-2003 and AGAGE SIO-14 calibration scales; we increased the AGAGE measurements by 10.38% following the known calibration offset between results for this chemical in these networks (Claxton et al., 2020). It is worth mentioning that AGAGE network uses in situ measurement systems, while the NOAA network uses flasks, which are transported and analyzed at the NOAA Global Monitoring Laboratory in Boulder, Colorado.

2.1.3. Auxiliary Data From ORCAS and CONTRAST

We complemented our analysis with Cl-VSLS observations from two additional field campaigns (Figure 1). We used CH_2Cl_2, $CHCl_3$, and C_2Cl_4 data measured by TOGA from the O_2/N_2 Ratio and CO_2 Airborne Southern Ocean Study (ORCAS) and the CONvective TRansport of Active Species in the Tropics (CONTRAST) missions, both deployed on the NSF/NCAR Gulfstream V (GV) aircraft. ORCAS was a 6-week study in 2016 (January–February) focused on the Southern Ocean (35–75°S) and collected data by frequently profiling the atmosphere up to ∼13 km altitude (Stephens et al., 2018). Similarly, during CONTRAST the GV profiled up to ∼15 km altitude during a 7-week study in 2014 (January–February), focusing on deep convection in the tropical western Pacific (20°S–40°N) (Pan et al., 2017).

2.2. Simulations

2.2.1. Model Configuration

CESM is a coupled climate/Earth system modeling framework with different components including land and atmosphere (Hurrell et al., 2013). CAM-chem, the Community Atmosphere Model with Chemistry, is the atmospheric component of CESM that solves the physics, dynamics, and chemistry of the troposphere and stratosphere (Lamarque et al., 2012). The online interaction between meteorology, thermodynamic processes, and chemistry makes CESM an appropriate model to study the global distribution and transport of VSLS (Wang, Kinnison, et al., 2019). The version of CAM-chem (based on CESM1) used in this study is based on the Community Atmosphere Model, version 4 (Neale et al., 2013; Tilmes et al., 2016), in which the hydroxyl radical (OH) abundance is calculated online (i.e., not prescribed). The horizontal resolution is 0.9° × 1.25° (latitude × longitude) with 56 vertical levels in a hybrid sigma-pressure system. The top boundary of the model is at 3 hPa (≈40 km).

We ran the model for 3 years 2016–2018 (after 2 years of spin-up) in specified dynamics mode, in which the temperature and horizontal winds are nudged with a 50-hr relaxation time toward data from NASA's Modern-Era Retrospective analysis for Research and Applications, Version 2 (MERRA-2) (Gelaro et al., 2017). The anthropogenic emissions are from the Copernicus Atmosphere Monitoring Service global emission inventory version 5.1 (CAMSv5.1) and Coupled Model Intercomparison Project Phase 6 (Granier et al., 2019; Hoesly et al., 2018), biomass burning emissions are from the Fire Inventory from NCAR, version 2.5 (FINN v2.5) based on MODIS fire detections (Wiedinmyer et al., 2023), and emissions from vegetation are calculated online in the land component of the model (CLM) based on the Model of Emissions of Gases and Aerosols from Nature (MEGAN; Guenther et al. (2012)). For CH_2Cl_2 and C_2Cl_4 emissions, we used the recently developed emission inventory by Claxton et al. (2020). They constrained the long-term global emissions of these two species up to 2017 (with no seasonality) based on a combination of long-term observation data, recent bottom-up emissions for Asia, and Reactive Chlorine Emissions Inventory (RCEI) framework for other regions, which led to improved modeling results (we extrapolated the emissions for the year 2018). The RCEI was a pioneering effort to produce the gridded global emission inventory of chlorinated species, which enabled assessment of atmospheric chlorine cycle (Keene et al., 1999). A latitude-dependent lower boundary condition (LBC) for $CHCl_3$ and 1,2-DCA was prescribed with higher values in the NH (Hossaini et al., 2016).

The tropospheric and stratospheric chemistry scheme is based on the MOZART-4 chemical mechanism implemented in CAM4-chem (Emmons et al., 2010; Kinnison et al., 2007; Tilmes et al., 2016). In addition, we used an updated VSLS chemistry scheme that includes the four Cl-VSLS, specifically CH_2Cl_2, C_2Cl_4, $CHCl_3$, and 1,2-DCA. This scheme is based on the halogen chemistry mechanism implemented by Ordóñez et al. (2012) and includes updates on halogen heterogeneous reactions and rate constants (Fernandez et al., 2014; Li et al., 2022; Saiz-Lopez et al., 2014). These updates will be included in the upcoming CESM2.3 release. The photochemical destruction pathways for the four Cl-VSLS are through reactions with OH and chlorine atom (Cl) and photolysis ($h\nu$) as shown below (R1–R12) (Hossaini et al., 2016).

CH_2Cl_2:

$$CH_2Cl_2 + h\nu \rightarrow 2Cl + \text{products} \quad \text{(R1)}$$

$$CH_2Cl_2 + OH(+O_2) \rightarrow CHCl_2O_2 + H_2O \quad \text{(R2)}$$

$$CH_2Cl_2 + Cl(+O_2) \rightarrow CHCl_2O_2 + HCl \quad \text{(R3)}$$

C_2Cl_4:

$$C_2Cl_4 + h\nu \rightarrow 4Cl + \text{products} \quad \text{(R4)}$$

$$C_2Cl_4 + OH \rightarrow 0.47COCl_2 + 3.06Cl + \text{products} \quad \text{(R5)}$$

$$C_2Cl_4 + Cl + M \rightarrow 5Cl + \text{products} \quad \text{(R6)}$$

$CHCl_3$:

$$CHCl_3 + h\nu\,(+O_2) \rightarrow CHCl_2O_2 + Cl \quad \text{(R7)}$$

$$CHCl_3 + OH \rightarrow COCl_2 + Cl + H_2O \quad \text{(R8)}$$

$$CHCl_3 + Cl \rightarrow COCl_2 + Cl + HCl \quad \text{(R9)}$$

1,2-DCA:

$$CH_2ClCH_2Cl + h\nu\,(+O_2) \rightarrow 2Cl + \text{products} \quad \text{(R10)}$$

$$CH_2ClCH_2Cl + OH \rightarrow 2Cl + H_2O \quad \text{(R11)}$$

$$CH_2ClCH_2Cl + Cl \rightarrow 2Cl + HCl \quad \text{(R12)}$$

2.2.2. Tagged Species

Tagged tracers are artificial emitted species treated as the replica of original tracers, going through similar reactions in the chemical mechanism and continuity equations as the original tracers, while not affecting the interactive

chemistry of the atmosphere (Emmons et al., 2012). To study different source regions' contributions to the atmospheric abundance of anthropogenic Cl-VSLS, we tagged CH_2Cl_2 and C_2Cl_4 emissions in the model simulation. Note that $CHCl_3$ and 1,2-DCA were based on LBC in this work and hence not tagged. We tagged CH_2Cl_2 and C_2Cl_4 emitted from Asia (AS), Europe (EU), North America (NA), South America (SA), and Africa (AF). Additionally, we assigned emissions outside these regions as the rest of the world (ROW) tracers. As a result, we implemented a total of 12 tagged tracers in the model. The emission magnitudes from each region of the tagged tracer was equal to the emission of that specific region in the original tracer emission inventory. Figure S1 in Supporting Information S1 shows that AS emissions are the dominant emission source of CH_2Cl_2 while AS, EU, and NA emissions of C_2Cl_4 are of the same order of magnitude. These tagged emissions go through photolysis, reaction with OH, and reaction with Cl. The primary source of inorganic chlorine in the model is through the heterogeneous reactions of halogenated species and sea salt aerosol (SSA) as well as mobilization of Cl^- from SSA through acid displacement (following Li et al., 2022). We use these emissions to estimate the tropospheric Cl-VSLS budgets due to different sources.

3. Results and Discussion

3.1. Vertical and Spatial Distribution of Cl-VSLS

The vertical profiles of measured CH_2Cl_2, C_2Cl_4, $CHCl_3$, and 1,2-DCA mixing ratios in different latitude bins for all the samples analyzed during ATom-1 through ATom-4 are shown in Figure 2 (vertical profiles for individual ATom deployments are shown in Figures S2–S5 in Supporting Information S1). In this section, we focus only on the measured data and different instruments, and the model performance is discussed in Section 3.3. The general trend for all the species is that the mixing ratios in the NH are higher than the SH. For example, the average (± standard deviation) of the measured CH_2Cl_2 mixing ratios by TOGA, within the vertical profile and all latitudes of the NH and SH (including their subtropical regions), were 59 ± 22 and 26 ± 7 ppt, respectively. Hossaini et al. (2017) found the NH to SH ratio (NH/SH) of 3 in mid-latitudes for CH_2Cl_2, based on data from ground measurement networks, which is within the in situ NH/SH possible range of our TOGA measurements (1.1–4.3).

Similarly, for C_2Cl_4, the mean mixing ratios in the NH and SH were 1.1 ± 0.6 and 0.3 ± 0.2 ppt, respectively. These C_2Cl_4 mixing ratios are significantly lower than those reported in the 20th century (Simmonds et al., 2006), consistent with its declining emission trend (Claxton et al., 2020). For example, Wiedmann et al. (1994) reported mean NH and SH C_2Cl_4 values of 21 ± 5 ppt and 2.2 ± 0.5, respectively, for the period between 1982 and 1989. TOGA data for 1,2-DCA (during ATom-4) shows mixing ratios of 12 ± 7 and 2 ± 1 in NH and SH, respectively, supporting the idea of their predominant NH sources, which are believed to be dominated by anthropogenic sources (Laube et al., 2022; Oram et al., 2017).

The interhemispheric gradient is also apparent for $CHCl_3$ with an NH/SH ratio of ∼2 (1–3.1) during ATom for TOGA data. While anthropogenic sources (i.e., solvents in the industrial sector) are the main source of CH_2Cl_2, 1,2-DCA, and C_2Cl_4 emissions, these sources have historically accounted for less than 30% of emitted $CHCl_3$ (Worton et al., 2006) although a larger anthropogenic contribution is more recently reported (Fang et al., 2019). An increase in NH anthropogenic emissions of $CHCl_3$ between 2011 and 2017 (and a decrease after 2018) was also reported in SAOD-2022 (Laube et al., 2022).

There are also regional differences for the Cl-VSLS, primarily over the NH mid-latitudes. Figure 3 shows the altitude dependence of Cl-VSLS differences measured over the Pacific and Atlantic Oceans (Pacific minus Atlantic), in 1-km altitude bins. Our measurements show that the NH mixing ratios over the Pacific Ocean are in general higher than those over the Atlantic Ocean. This enhancement is strongest for CH_2Cl_2 with a difference of up to 18 ppt in the mid-troposphere. In addition, the results show a seasonal difference. For example, the results for ATom-2 (May 2017) and ATom-3 (October 2017) are the extremes of the measured differences, in particular for C_2Cl_4 and $CHCl_3$, meaning the smallest and largest differences occurred during these two deployments (see Figures 3b and 3c).

3.1.1. CH_2Cl_2

For CH_2Cl_2 in the northern high-latitude region (55–90°N), measurements indicate that the atmosphere is well mixed in the troposphere and there is a strong vertical gradient in the UTLS region. In the northern mid-latitudes (20–55°N), the measured data show a smooth vertical gradient, where the median TOGA measurements decreased, overall, by 1.3 ppt km^{-1} with increasing altitude in contrast with 2.5 ppt km^{-1} in the high latitudes

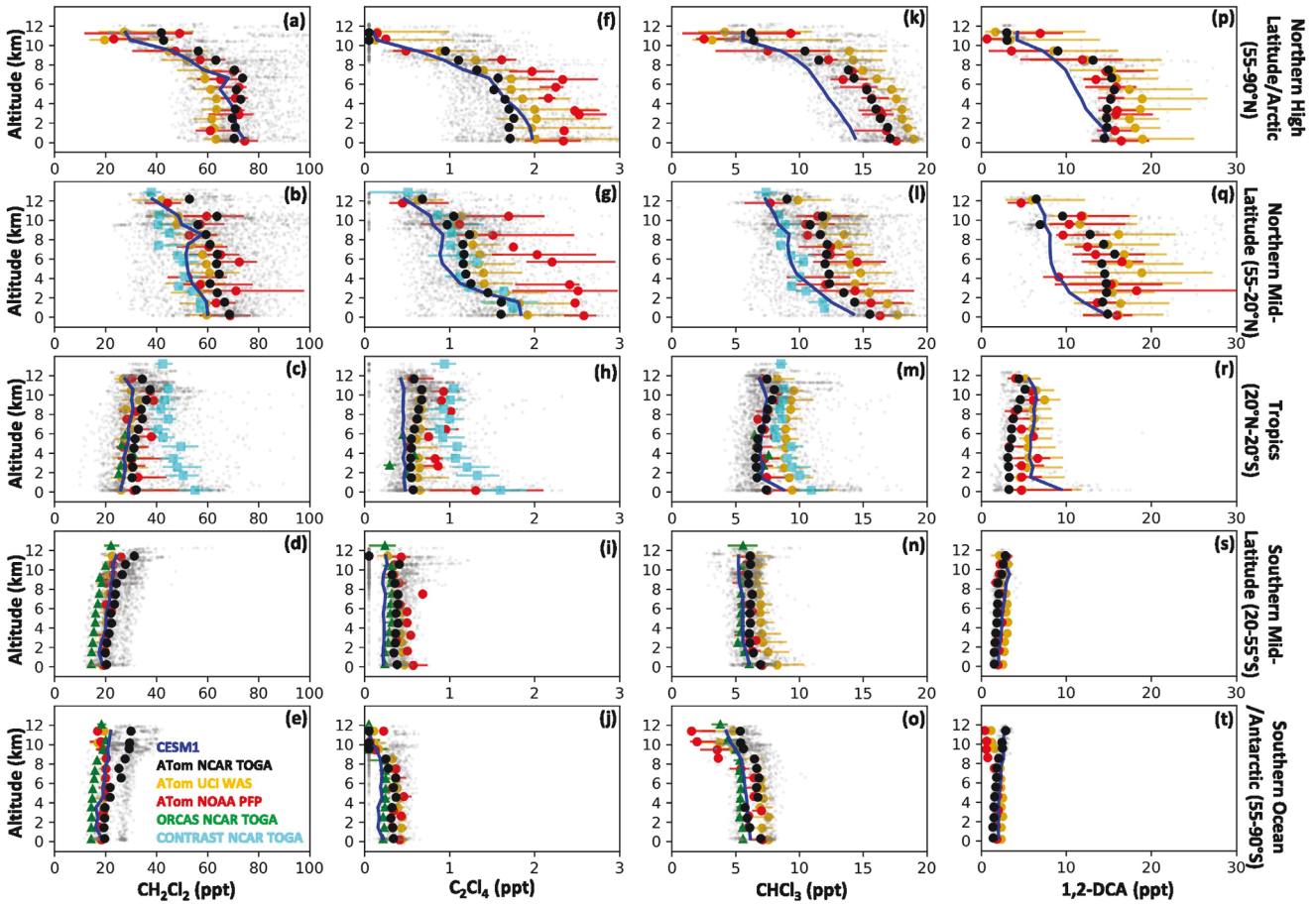

Figure 2. Binned vertical profiles of median measured CH_2Cl_2, C_2Cl_4, $CHCl_3$, and 1,2-DCA mixing ratios for all ATom deployments from TOGA (black), WAS (gold), and PFP (red), separated into five different latitude bins; 55–90°N (a, f, k, p), 20–55°N (b, g, l, q), 20°S–20°N (c, h, m, r), 55–20°S (d, i, n, s), and 90–55°S (e, j, o, t), accompanied by the vertically binned median CESM1 model results sampled along the ATom flight tracks (blue curve). Note that C_2Cl_4 data for PFP (red points) are only available for ATom-4. Additionally, 1,2-DCA data for PFP are for ATom-2 to ATom-4 and for TOGA are only for ATom-4—see Figures S2–S5 in Supporting Information S1 for individual deployments. Vertically binned median TOGA measurements made during ORCAS (green) and CONTRAST (cyan) are also shown. Individual ATom TOGA data points are included (light gray points) although the *x*-axes are limited for better clarity in the SH plots. Error bars for PFP, WAS, CONTRAST, and ORCAS data are the 25th to 75th percentiles.

(the mean slope is calculated based on lowest and highest altitude bins). It should be noted that the slopes differ for each ATom deployment (Figure S2 in Supporting Information S1). The model captured the seasonal pattern for each ATom deployment (note that emissions do not have seasonality (Claxton et al., 2020)), suggesting that OH abundances control the seasonal trend (i.e., R2 is the main photochemical destruction pathway for CH_2Cl_2

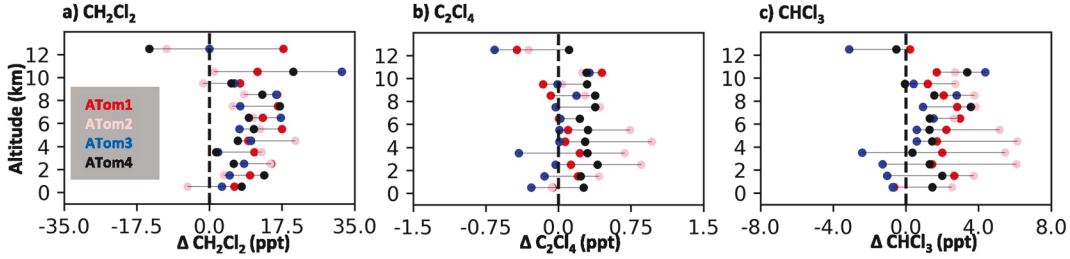

Figure 3. Vertical profiles of the median Pacific minus median Atlantic mixing ratios for (a) CH_2Cl_2, (b) C_2Cl_4, and (c) $CHCl_3$ from the TOGA observations at northern mid-latitudes (20–55°N). Marker colors show the differences during ATom-1 (red), ATom-2 (pink), ATom-3 (blue), and ATom-4 (black); negative values indicate that median mixing ratios over the Atlantic were larger than the Pacific. Note the horizontal gray lines only connect the points for better visualization and do not show the range of the observations.

as will be discussed in Section 3.5). Similarly, Claxton et al. (2020) found that their constant monthly emissions were able to generate CH_2Cl_2 seasonality. In the tropics, the CH_2Cl_2 levels are about half of the values for the NH mid- and high latitudes. In addition, the observed tropical mixing ratios are higher at upper altitudes such that the maximum median CH_2Cl_2 value in the profile was at ∼10 km. The relatively high mixing ratios in the upper troposphere and reversal of the vertical gradient in the tropics suggest influential impacts of atmospheric dynamics (i.e., transport and convection), pointing to the interhemispheric transport from NH to SH. Similarly in the southern mid-latitudes (20–55°S) and over the Southern Ocean (55–90°S) TOGA CH_2Cl_2 mixing ratios were higher in the upper troposphere than the lower troposphere (inversion with slope ∼−0.9 ppt km^{-1}, where a negative slope indicates increasing levels with increasing height).

The CH_2Cl_2 observations from all three instruments (TOGA, WAS, and PFP) compare quite well with each other (Figures 2a–2e) and lead to a similar conclusion although there are some minor differences in some regions. For example, in the high-latitude Arctic region (Figure 2a), the vertically binned median CH_2Cl_2 values from TOGA and PFP are in good agreement with each other yet the WAS data are about 10 ppt lower throughout the profile. The comparisons differ somewhat for each ATom deployment (Figure S2 in Supporting Information S1). Specifically, during ATom-2, the medians for all three instruments were about 10 ppt from each other within the marine boundary layer (MBL) and very close in the UTLS region. On the other hand, during ATom-3 the median for WAS and PFP CH_2Cl_2 levels were consistent while TOGA was as much as 15 ppt higher. In addition, TOGA and WAS agreed well during ATom-4 while PFP was on the higher end of the measurements. Some additional inconsistencies were observed between TOGA and the flask measurements from PFP and WAS over the southern high latitudes. TOGA measurements above 8 km over the Southern Ocean increased with altitude while WAS and PFP measurements showed a decrease, leading to large biases (e.g., the CH_2Cl_2 mixing ratio within the 10-km bin (10–11 km altitude) during ATom-4 was 31.5 and 13.8 ppt measured by TOGA and WAS, respectively). As will be discussed in Section 3.3, the model also showed a modest increase, which is consistent with TOGA data although the TOGA data showed a substantially larger increase.

3.1.2. C_2Cl_4

C_2Cl_4 mixing ratios are very low (<5 ppt) everywhere. Nevertheless, C_2Cl_4 has vertical and spatial gradients similar to CH_2Cl_2. At high latitudes, median TOGA measurements show a smooth gradient in the troposphere, and transition to below LLOD with a strong gradient in the UTLS region. Similarly, both WAS and PFP measured very small C_2Cl_4 levels in the UTLS region. However, Figure 2 shows fairly significant differences that are most pronounced in the NH between PFP and the other two instruments that measured C_2Cl_4, even when only ATom-4 results are considered. This may be due to differences in calibration scales, which we have not pursued further in this work, and may relate to Teflon O-ring contamination of some PFP flask data. It is worth noting that PFP results were reported for C_2Cl_4 only during the ATom-4 deployment (Figure S3 in Supporting Information S1). In northern mid-latitudes, the median TOGA C_2Cl_4 levels decreased with increasing altitude down to 0.7 ppt above 10 km. In the tropics, median high-altitude C_2Cl_4 mixing ratios were slightly higher than at low altitudes. However, the median data during the ATom mission (for all three measurement systems) did not show an inverted vertical gradient in the SH. Nevertheless, a wider range of mixing ratios (gray dots) was seen at high altitudes in the southern mid-latitudes (Figure 2i) with mixing ratios reaching >1 ppt, suggesting an inversion, with less intensity but similar to CH_2Cl_2 data.

3.1.3. $CHCl_3$

The observed $CHCl_3$ mixing ratios also showed a vertical gradient in the NH (Figures 2k and 2l). However, unlike the predominantly anthropogenically emitted CH_2Cl_2 and C_2Cl_4, the low-altitude $CHCl_3$ levels are modestly higher in the NH high latitudes compared with the mid-latitudes. Specifically, TOGA $CHCl_3$ levels below 3 km in the 60–90°N latitude bin were 8% higher than in the 30–60°N latitude bins, with the highest differential measured during ATom-1 (18%). This is in contrast to constant $CHCl_3$ mixing ratios between 30 and 90°N shown by Prinn et al. (2000), which is used in our model. The global emissions of $CHCl_3$ showed a rapid increase between 2010 and 2017 (Laube et al., 2022), which is attributed to anthropogenic emission increases in China (An et al., 2023; Fang et al., 2019). On the other hand, $CHCl_3$ has major natural sources with higher emissions in the mid-latitude regions (Khalil & Rasmussen, 1999). The combined impact of transport of emissions (natural and anthropogenic) and distribution of natural emissions could explain, in part, the higher mixing ratios at 60–90°N. In the tropics, TOGA observed a declining gradient within the MBL, with increasing altitude, and an increasing gradient at higher altitudes (i.e., change of the gradient sign), similar to what was observed for CH_2Cl_2 and C_2Cl_4. This inverted "S" shape profile has been also observed for

Table 2
Summary of TOGA-Observed Median Mole Fractions (and 10th–90th Percentiles) for Four Cl-VSLS and Total Cl^{VSLS} During ATom Within Different Latitude and Altitude Bins

Latitude region	Potential temperature θ (K)	CH_2Cl_2[a], ppt	C_2Cl_4[a], ppt	$CHCl_3$[a], ppt	1,2-DCA[b], ppt	Σ Cl^{VSLS} [c], ppt
Northern High Latitudes/Arctic	<320	70.2 (54.1–91.6)	1.5 (1.0–2.4)	15.3 (11.4–18.7)	14.8 (12.6–18.2)	206.4 (150.0–251.2)
	320–340	59.4 (41.3–94.7)	1.1 (LLOD–1.60)	11.4 (6.6–15.3)	11.1 (4.0–15.9)	166.1 (105.0–244.3)
	340–360	33.8 (25.9–46.3)	LLOD	5.2 (4.2–6.6)	2.9 (2.4–4.1)	86.7 (66.8–119)
	360–380	41.6 (33.1–57.5)	LLOD	5.8 (4.8–8.1)	3.1 (2.5–3.4)	106.6 (85.3–139.3)
Northern Mid-latitudes	<320	66.2 (45.4–81.7)	1.4 (0.8–2.3)	14. (9.2–17.9)	14.7 (9.8–20.5)	189.9 (129.2–234.1)
	320–340	59.2 (39.7–96)	1.1 (0.6–1.6)	11.5 (7.8–15.2)	11.7 (5.7–27.4)	162.9 (107.2–258.7)
	340–360	41.6 (34.2–67.3)	0.7 (LLOD–1.1)	8.3 (6.7–10.6)	6.5 (3.5–16.5)	110.8 (93.6–171.5)
	360–380	N.A.[d]	N.A.	N.A.	N.A.	N.A.
Tropics	<320	31.1 (21.1–59.5)	0.6 (0.3–1.4)	7.1 (5.5–12.3)	3.3 (1.8–11.3)	86.4 (63.7–166.3)
	320–340	33.2 (23.4–48)	0.6 (0.4–1.0)	7.2 (5.8–9.8)	3.6 (2.5–6.6)	91.7 (69.5–130.2)
	340–360	35.7 (27.3–47.5)	0.6 (0.4–0.9)	7.7 (6.3–10.0)	4.8 (2.9–5.7)	99.6 (76.7–130.5)
	360–380	N.A.	N.A.	N.A.	N.A.	N.A.
Southern Mid-latitudes	<320	21.9 (16.1–28.7)	0.4 (LLOD–0.51)	6.3 (5.1–7.6)	1.7 (1.3–2.1)	65.2 (51.9–80.4)
	320–340	27.4 (20.8–33.6)	0.4 (LLOD–0.6)	6.0 (4.6–6.9)	2.5 (2.0–3.0)	75.9 (58.8–88.8)
	340–360	30.5 (22.7–39.7)	0.5 (LLOD–0.8)	6.1 (4.3–7.6)	3.2 (2.9–3.4)	81.2 (61.2–102.2)
	360–380	25.6 (22.4–27.9)	LLOD	3.6 (3.2–4.7)	N.A.	61.5 (55.5–70.2)
Southern Ocean/ Antarctic	<320	24.8 (16.7–30.8)	0.3 (LLOD–0.5)	6.5 (5.1–7.7)	1.6 (1.3–2.3)	71.2 (51.4–83.9)
	320–340	29.1 (22.5–35.5)	LLOD (LLOD–0.4)	5.3 (3.8–5.9)	2.4 (2.0–2.9)	76.7 (58.8–91.1)
	340–360	34.2 (23.4–39.5)	LLOD	4.9 (3.5–6.0)	2.8 (2.3–3.2)	87.6 (57.5–102.5)
	360–380	29.3 (24.3–39.9)	LLOD	4.6 (3.3–5.9)	3.0 (2.3–3.4)	73.4 (60.2–104.9)

[a]The reported values for CH_2Cl_2, C_2Cl_4, and $CHCl_3$ are based on TOGA data for all ATom deployments. [b]1,2-DCA is only available from TOGA for ATom-4. [c]Total Cl atoms from the sum of available chlorine in CH_2Cl_2, $CHCl_3$, C_2Cl_4, and 1,2-DCA. [d]N.A. = data not available.

brominated compounds during the CONTRAST mission and was attributed to the convective and advective transport from the surface to the free troposphere (Butler et al., 2018). In the SH, the overall trend suggests a small decreasing gradient although it differs for individual ATom deployments. For example, in the southern mid-latitudes, TOGA measured a decreasing vertical gradient during ATom-1 and ATom-3, and an increasing vertical gradient during ATom-2 and ATom-4. Measurements by WAS and PFP were, in general, consistent with TOGA although WAS reported up to 30% higher mixing ratios during ATom-1 compared with the other two instruments.

3.1.4. 1.2-DCA

The measurements of 1,2-DCA mixing ratios show significant enhancements in the NH (Figure 2). In addition, the similar vertical profile shape of 1,2-DCA and CH_2Cl_2 suggests their emission sources are co-located with each other (Oram et al., 2017). Similar to CH_2Cl_2, the Southern Ocean vertical profile of 1,2-DCA between TOGA, WAS, and PFP are different (Figure 2t). The vertical profiles of measured 1,2-DCA for each deployment are in Supporting Information S1 (Figure S5). The SAOD-2018 reported 1,2-DCA as the second most abundant anthropogenic Cl-VSLS, after CH_2Cl_2, in the tropical MBL with a median of 12.8 ppt based on measurements during CAST and CONTRAST in 2013–2014 (Andrews et al., 2016; Engel et al., 2018; Pan et al., 2017). TOGA measurements, Table 2, show that 1,2-DCA mixing ratios during ATom (e.g., 1.8–11.3 ppt in the tropical MBL) are lower than that of $CHCl_3$ (e.g., 5.5–12.3 ppt in tropical MBL). Our observations with lower levels of 1,2-DCA compared to $CHCl_3$ may be due to the region studied during CAST and CONTRAST being further west (and closer to the emission sources) and the shorter atmospheric lifetime of 1,2-DCA compared to $CHCl_3$, or due to either decreasing 1,2-DCA emissions or increasing $CHCl_3$ emissions or a difference in measurement calibration.

3.1.5. Total Chlorine During ATom

Overall, there is reasonable agreement between TOGA, PFP, and WAS Cl-VSLS measurements during the ATom mission. In particular, all the measurements agreed within the reported uncertainties. Nevertheless, TOGA provided better data coverage than PFP and WAS as was mentioned in the methods section. As a result, we only use TOGA measurements for the remainder of this paper. The measured TOGA annual global mean mixing ratios ± standard deviations for CH_2Cl_2 (46.6 ± 24.2 ppt), $CHCl_3$ (9.6 ± 4.2 ppt), 1,2-DCA (7.8 ± 7.3 ppt), and C_2Cl_4 (0.84 ± 0.66 ppt) confirm that CH_2Cl_2 is the most abundant Cl-VSLS in the atmosphere. Table 2 summarizes the TOGA-measured anthropogenic Cl-VSLS and total VSLS-sourced chlorine, Cl^{VSLS}, during the ATom mission for different latitude bins and altitude ranges (represented by potential temperature, θ). Here, total Cl^{VSLS} is calculated based on the available chlorine from major Cl-VSLS ($CHCl_3$, CH_2Cl_2, C_2Cl_4, and 1,2-DCA). In the NH and tropics, the highest amount of total Cl^{VSLS} was observed within the MBL (i.e., $\theta < 320$ K). However, the highest values in the SH were found in the upper troposphere (i.e., $\theta > 340$ K), suggesting an interhemispheric transport as discussed below. Within the tropical upper troposphere, the median total Cl^{VSLS} (and range) was 99.6 (76.7–130.5) ppt. Table S3 in Supporting Information S1 summarizes the ATom measured mole fractions of ClVSLS, in the tropical upper troposphere, alongside the reported values in the literature (Adcock et al., 2021; Oram et al., 2017; Laube et al., 2022. SAOD-2022). Both the total Cl^{VSLS} and the median mixing ratios of individual Cl-VSLS (i.e., CH_2Cl_2, C_2Cl_4, and $CHCl_3$) in the tropics (Table S3 in Supporting Information S1) are close to the range of the reported values in the SAOD-2022 report (Laube et al., 2022). However, the differences for 1,2-DCA were large; ATom data (median of 4.8 ppt) were about 40% lower than SAOD (2022) data (median of 8.3 ppt). On the other hand, the upper bound of measurements in South and East Asia (Adcock et al., 2021; Oram et al., 2017) were significantly high, as they were close to the source regions. For example, the upper bound of CH_2Cl_2 mixing ratios were 136 ppt in South Asia (Adcock et al., 2021), in contrast with 47.5 ppt measured during ATom.

3.1.6. Uncertainties Between Instruments

As discussed above, there are some locations with poor agreement between the Cl-VSLS measured by the three instruments, in particular over the Southern Ocean. From our analysis using the five latitude bins shown in Figure 2, the Southern Ocean bin had the lowest average temperatures and water vapor mixing ratios. Above 8 km, the average temperature was 214.8 K and the average water vapor mixing ratio was 25.9 ppm. The latitude bin with next lowest mean water vapor mixing ratio was over the northern high latitudes at 56.2 ppm followed by the southern mid-latitudes at 153.0 ppm.

One hypothesis for the instrumental differences is that the measurement biases could be due to losses on either the unheated inlet walls or the canister/flask walls for the WAS and PFP measurements, which can be more pronounced at lower ambient humidities.

TOGA uses a heated Sulfinert™ inlet line and does not store the samples prior to analysis. The flask samples (WAS and PFP) are collected by drawing air in through non-heated lines; WAS uses a non-heated stainless steel (SS) line and the PFP uses a coated SS line. For most materials, a threshold level of humidity is needed to keep surfaces properly passivated. Exceptions are in the case of Teflon™ or Silonite™ (Deming et al., 2019) for which there is little absorptive effect even at 0% humidity. Glass and SS also showed to be relatively non-adsorptive although not as good as Teflon™ or Silonite™. In the Deming et al. (2019) study, Sulfinert™ tubing was not tested but Silonite™, which is believed to be a very similar product, was tested. The UCI WAS uses SS canisters that are humidified, thus potentially mitigating absorptive losses on the canister surfaces. The PFP glass flasks have been tested for long-term storage of VSLS in surface-air samples collected under a wide variety of humidity levels and storage times and no issues have been found for CH_2Cl_2 measurements. An alternative hypothesis to explain measurement discrepancies is that TOGA had a sampling artifact at these low humidities and that the canister/flask measurements are more accurate. The rational for this hypothesis is that subtropical jets in the UTLS region inhibits the horizontal transport of tracers, leading to small values measured by UCI WAS and PFP (Jesswein et al., 2022). One problem with this hypothesis is that there would have to be a mechanism for artifact formation in the TOGA analytical system that would result in higher CH_2Cl_2 and 1,2-DCA mixing ratios in this region than were actually present and to date we have not seen evidence of artifact formation for this species. Additionally, better correlation between the model and TOGA results increases the likelihood of our first hypothesis.

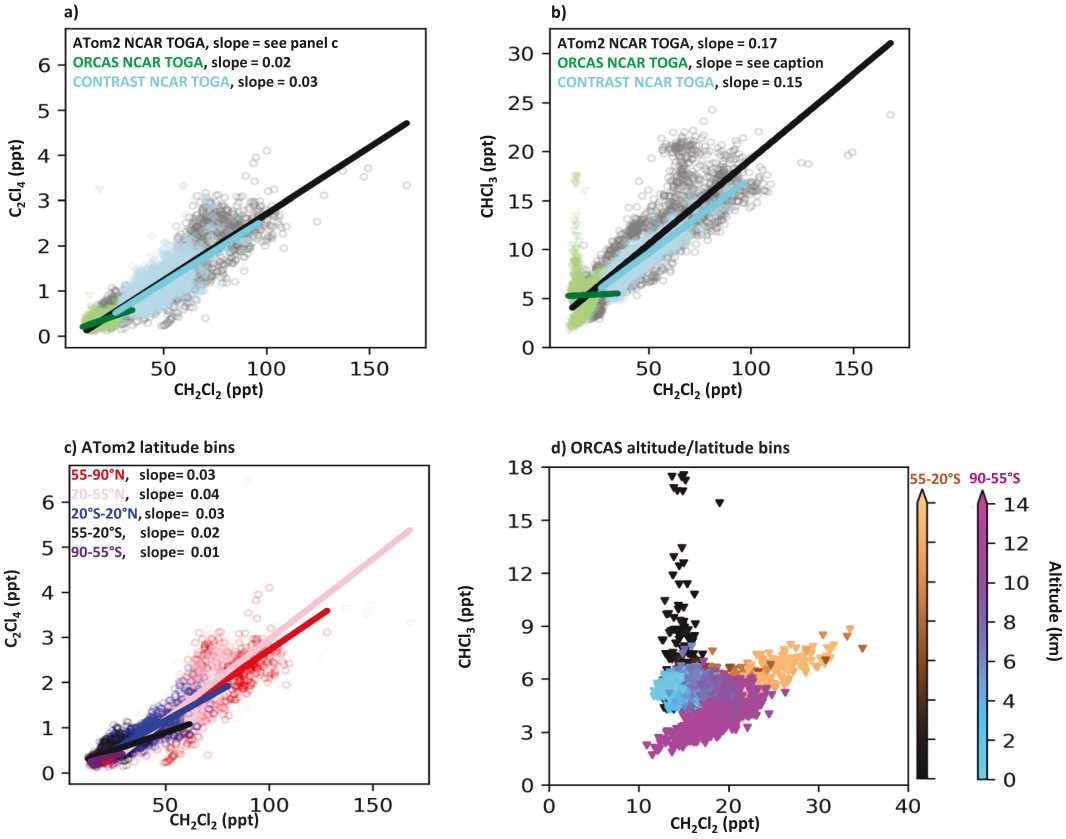

Figure 4. Correlation plots of Cl-VSLS measured by TOGA for (a) C_2Cl_4 versus CH_2Cl_2 and (b) $CHCl_3$ versus CH_2Cl_2 from ATom-2, ORCAS, and CONTRAST, (c) C_2Cl_4 versus CH_2Cl_2 from ATom-2, colored by latitude bins, and (d) $CHCl_3$ versus CH_2Cl_2 from ORCAS colored by latitude bin and shaded by altitude. Lines show least square linear regressions. Note that although a line is shown for $CHCl_3$ versus CH_2Cl_2 from ORCAS in (b), regional data in (d) indicate a non-linear relationship. Note that the axes are different in each panel. Note also that only ATom-2 data are considered in this analysis to match the seasons with the CONTRAST and ORCAS projects.

3.2. Cl-VSLS Abundance in Different Field Studies

Cl-VSLS were also measured by TOGA during ORCAS and CONTRAST. These two missions as well as the ATom-2 deployment occurred primarily during the month of February in different years previous to ATom. The vertical profiles of CH_2Cl_2, $CHCl_3$, and C_2Cl_4 from ORCAS and CONTRAST are also shown in Figure 2 (and Figures S2–S4 in Supporting Information S1). Both ORCAS and ATom sampled air from similar regions in the SH (Figure 1) but different years and the similar shape of the vertical profiles (in Figures S2–S4 in Supporting Information S1) shows small interannual variability of the Cl-VSLS mixing ratios. On the other hand, the CONTRAST mission sampled air masses in the western tropical Pacific region closer to Asia, which led to higher mixing ratios compared with the ATom data (Figures S2–S4 in Supporting Information S1). In addition, the vertical profiles for the CONTRAST Cl-VSLS had sharper gradients in the MBL compared with ATom data, suggesting that low-level outflow from the Asian continent was sampled. Also, the fast convection over the Pacific increases the Cl-VSLS levels at higher altitudes.

Figure 4 shows correlations of observed C_2Cl_4 versus CH_2Cl_2 and $CHCl_3$ versus CH_2Cl_2 for ORCAS, CONTRAST, and ATom-2. It is worth mentioning that only ATom-2 is considered in this analysis to match the seasons. C_2Cl_4 versus CH_2Cl_2 for the ORCAS and CONTRAST regional missions are overlaid on ATom-2 global data and show similar positive correlations. In particular, the C_2Cl_4/CH_2Cl_2 ratio was 0.02 and 0.03 for the limited latitudinal-range ORCAS (Southern Ocean region) and CONTRAST (tropics) data, respectively. The C_2Cl_4/CH_2Cl_2 ratio for the global latitudinal-range ATom-2 data was 0.01–0.04, decreasing for SH latitude bins, suggesting less transported C_2Cl_4 in the SH or faster loss in the SH. We will analyze interhemispheric transport in more detail in Section 3.4. Figure 4 also shows similar tight positive correlations between $CHCl_3$ and CH_2Cl_2

during CONTRAST and ATom-2 data, while $CHCl_3$ does not correlate with CH_2Cl_2 in some of the ORCAS data. Within the Southern Ocean region, this was also seen in the ATom-2 data (Figure S6 in Supporting Information S1). As shown in Figure 4d, there are two clusters of data in the Southern Ocean/Antarctica latitude bins (55–90°S). One cluster contains low CH_2Cl_2 and relatively high $CHCl_3$ mixing ratios that are measured near the surface. We found positive correlation between near the surface $CHCl_3$ and two major oceanic tracers (CH_3I and $CHBr_3$) during ORCAS, confirming the role of natural oceanic emissions of $CHCl_3$ in the Antarctic region (not shown). In contrast, the other cluster shows a positive correlation between $CHCl_3$ and CH_2Cl_2 at high altitudes. Since the lifetime of CH_2Cl_2 and $CHCl_3$ are of the same magnitude (Hossaini et al., 2019), the positive correlation suggests this cluster is being transported from other regions; that is, from the NH or tropics. The natural sources of $CHCl_3$ include both oceanic (macro and microalgae) and terrestrial (soil) sources, with more natural emissions in the NH than the SH (Laturnus et al., 2002). Nevertheless, the strong correlation between $CHCl_3$ and CH_2Cl_2, in particular in the tropics and NH (Figure S6 in Supporting Information S1), also suggests that maybe anthropogenic sources dominate $CHCl_3$ emissions sources. Fang et al. (2019) and An et al. (2023) have shown that the changes in anthropogenic emissions can explain the recent changes in global concentrations.

3.3. Evaluation of CESM1 Using ATom Measurements

Figure 2 includes the vertical profiles of median modeled Cl-VSLS species in CESM sampled along ATom flight tracks and corresponding to TOGA measurement times. Similar to the measurements, the model showed substantially higher Cl-VSLS mixing ratios in the NH. For CH_2Cl_2, the model captured the observed vertical gradients; that is, mixing ratios decreasing with increasing altitude in the NH and a slight vertical inversion (higher levels at higher altitudes) in the tropics and SH. The model captured the magnitude of the median surface layer (i.e., <1 km) CH_2Cl_2 mixing ratios in the high-latitude Arctic region, but was approximately 10 ppt lower than the measurements in the northern mid-latitudes. In addition, the modeled CH_2Cl_2 mixing ratios were lower than TOGA measurements in the tropics and SH throughout the troposphere. Overall, we report the NMB, RMSE, and r of −15%, 16 ppt, and 0.80, respectively, for modeled CH_2Cl_2 against TOGA measurements in all ATom deployments (Table S4 in Supporting Information S1). For C_2Cl_4, the model captured the surface mixing ratios over the extratropical regions in the NH. However, the model was biased low at higher altitudes in the northern mid-latitudes. Additionally, the model was biased low in the tropics and SH. The NMB, RMSE, and r for C_2Cl_4 are −7%, 0.5 ppt, and 0.82, respectively (Table S5 in Supporting Information S1). Our model used constant LBC values, rather than emissions, for $CHCl_3$ and 1,2-DCA. For $CHCl_3$, the model underestimated the concentrations with NMB, RMSE, and r of −17%, 3 ppt, and 0.85, respectively. Similarly for 1,2-DCA, the model underestimated its global abundance with NMB, RMSE, and r of −23%, 6 ppt, and 0.74, respectively. (Note that TOGA measured 1,2-DCA only during ATom-4). The model captured the Cl-VSLS mixing ratios in the tropics and SH, with UCI WAS generally showing higher values than TOGA and PFP. On the other hand, the model bias for $CHCl_3$ and 1,2-DCA was larger than CH_2Cl_2 and C_2Cl_4 over the NH high latitudes. Statistics for individual ATom deployments are also listed in Tables S4–S7 in Supporting Information S1. In the following sections, we look in more detail on model performance and transport of CH_2Cl_2 and C_2Cl_4, which have anthropogenic sources with well-constrained magnitudes (Claxton et al., 2020).

Figure 5 shows the measured and corresponding modeled profiles for CH_2Cl_2 and C_2Cl_4 mixing ratios for each ATom deployment, binned zonally (Figure S7 in Supporting Information S1 shows similar plots for $CHCl_3$ and 1,2-DCA, as well as the OH observed by the Pennsylvania State University Airborne Tropospheric Hydrogen Oxides Sensor, ATHOS). Both measurements and model output show strong seasonal differences for Cl-VSLS in the NH. For CH_2Cl_2, both the highest measured and modeled mixing ratios were over the NH high latitudes. However, the highest modeled values were for ATom-4 (May 2018) but the highest measured values were during ATom-2 (February 2017). In the NH, CH_2Cl_2 up to 100 ppt was measured during ATom-3 (October 2017), yet the model values only reached 60 ppt. Since the model is biased high for OH concentration (Figure S7 in Supporting Information S1), and Cl-VSLS lifetimes are a few months, the large bias of the model during ATom-3 could be due to the integrated impact of high-biased OH during the highest OH exposure period in the NH. The lowest modeled CH_2Cl_2 mixing ratios in the NH were for the ATom-1 (August 2016) period, consistent with the measurements. In addition, the model predicted a homogenous NH vertical gradient during ATom-1, which is also consistent with the measurements. For C_2Cl_4, both model and measurements agreed with the highest NH mixing ratios during ATom-2 (February 2017), although the model overestimates the mixing ratios (NMB of 24% in high-latitude Arctic region). Similar to CH_2Cl_2, the lowest NH C_2Cl_4 mixing ratios were during ATom-1, both

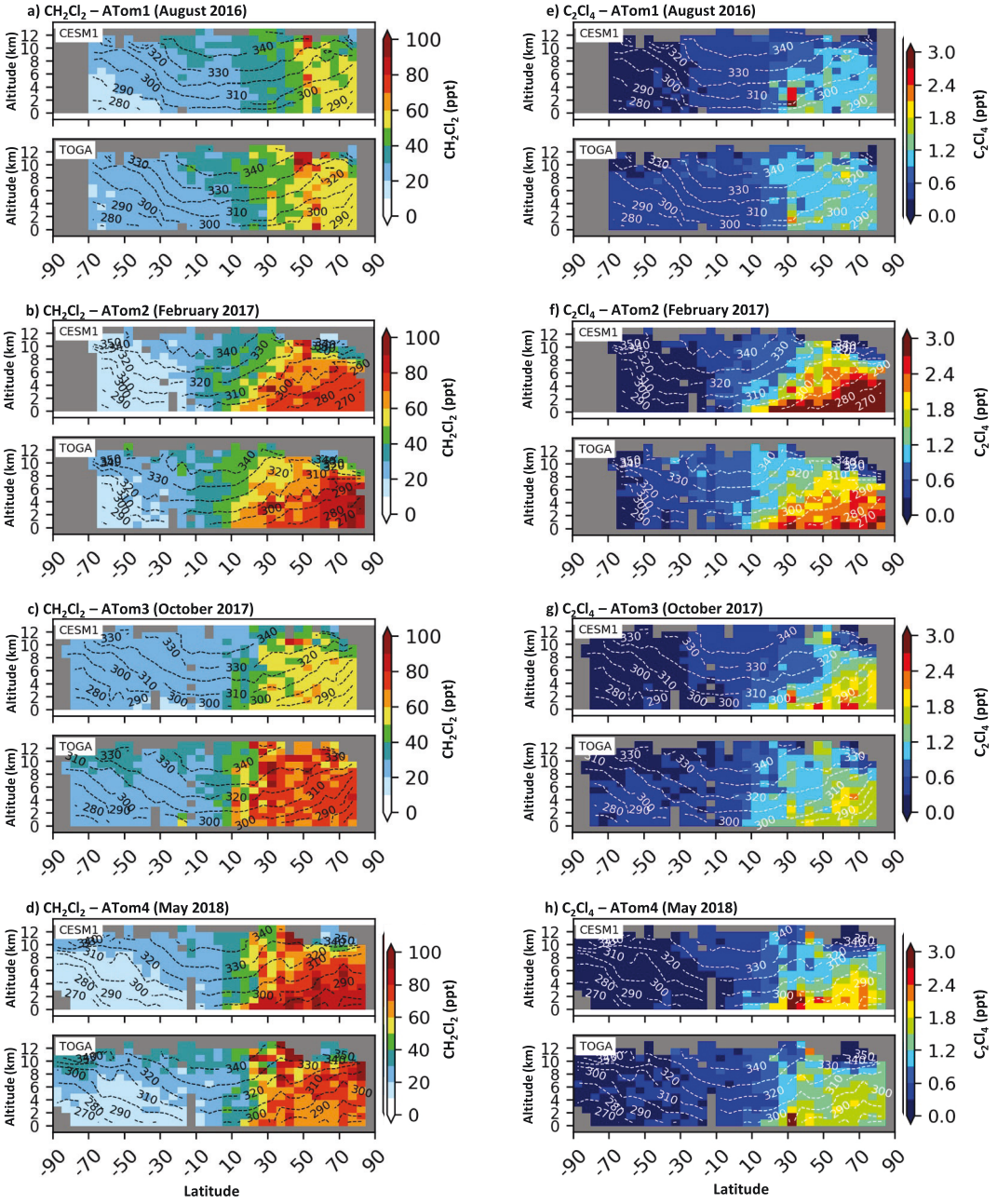

Figure 5. Spatially binned distribution of mean modeled (top subplot) and measured (bottom subplot) for (a–d) CH_2Cl_2 and (e–h) C_2Cl_4 mixing ratios during individual ATom deployments. Latitude and altitude bin intervals are 5° and 1 km, respectively. Corresponding TOGA sample locations for each ATom mission are shown in Figure S7 in Supporting Information S1.

measured and modeled. The high mixing ratios during ATom-2 (February 2017) and low mixing ratios during ATom-1 (August 2016) reveal seasonal differences for both CH_2Cl_2 and C_2Cl_4, which the model clearly captured. This seasonal variation can be explained primarily by OH seasonal variations, as the emissions in the model were constant throughout the year (Figure S7 in Supporting Information S1). In particular, lower [OH] during NH winter leads to greater Cl-VSLS abundance, with the opposite true in NH summer. In addition, atmospheric dynamics play a role in the observed mixing ratios. For example, the enhanced high-altitude Cl-VSLS mixing ratios measured in the NH mid-latitudes during ATom-1 are potentially due to the Asian Summer Monsoon deep convection. Wang et al. (2020) found that the CAM-chem model captured the large-scale processes during ATom-1 and ATom-2 including the isentropic mixing from low latitudes to high latitudes. Similar to Wang

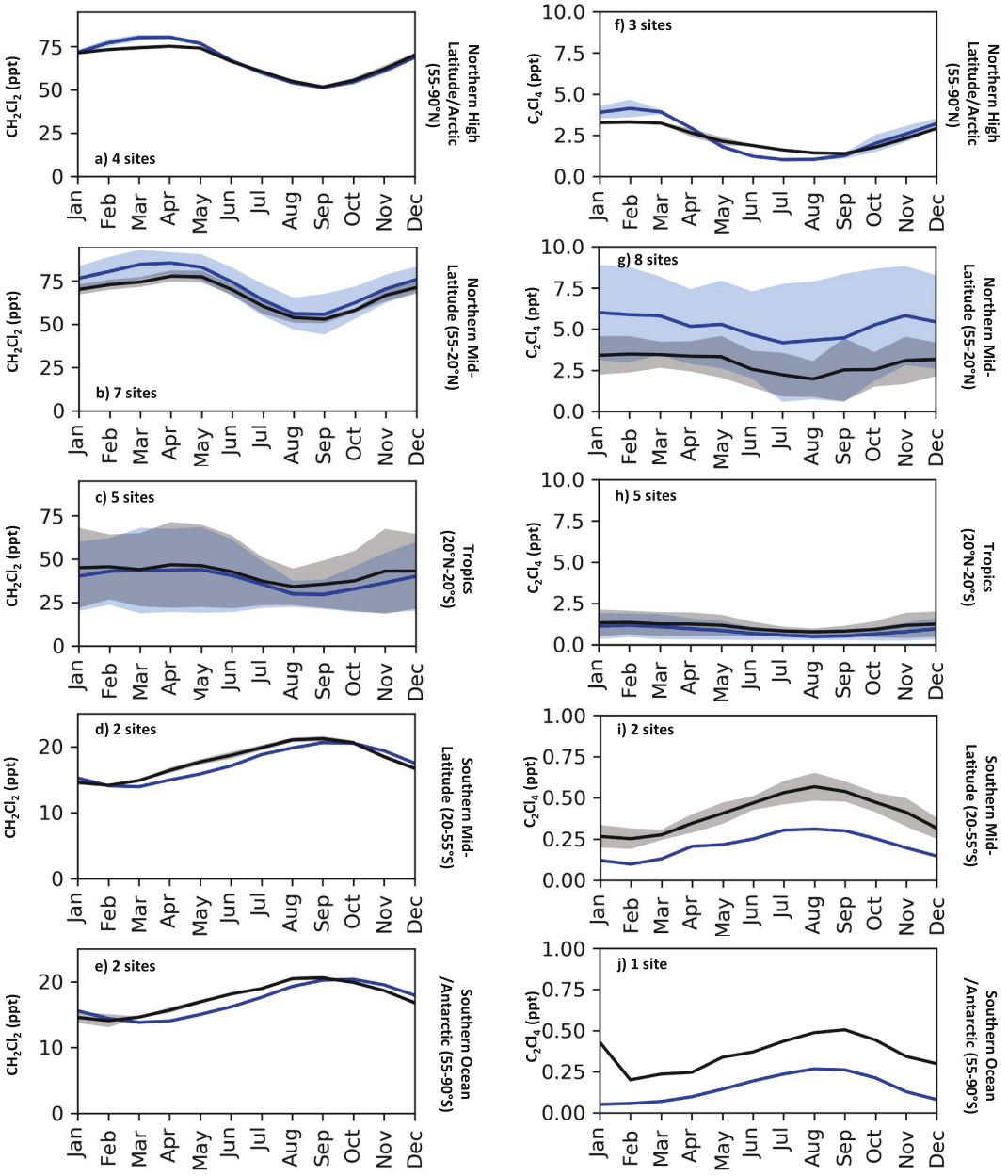

Figure 6. 2016–2018 monthly means of ground-based measurements (black) and corresponding modeled (blue) ± 1 standard deviation (shading) of CH_2Cl_2 and C_2Cl_4 mixing ratios over five different latitude bins: 55–90°N, 20–55°N, 20°S–20°N, 55–20°S, and 90–55°S. Ground-based measurements are from the stations within NOAA and AGAGE networks shown in Figure 1. The shading represents the ±1 standard deviation of the monthly means from multiple sites within each latitude range and not the spread over different years for individual sites. Note that for many months the standard deviations (both model and measurements) are very small compared with the *y*-axes scales. Also, note that smaller *y*-axes limits are used for SH panels.

et al. (2020), the wind fields and temperature in the model in this work are nudged toward the MERRA-2 reanalysis data to better capture the large-scale processes.

Figure 6 shows the monthly means of surface CH_2Cl_2 and C_2Cl_4 mixing ratios modeled and observed by ground measurement stations between 2016 and 2018 and using the corresponding model grid cells, divided into latitude bins. For CH_2Cl_2, the model overestimated the maximum in the observations in NH mid-latitudes during winter and spring and captured the minimum values during summer, and measurements were in the

range of modeled data. Over other regions, the model mostly underestimated the CH_2Cl_2 mixing ratios. The majority of stations were located in the tropics (five stations) and northern mid-latitudes (seven stations), where the spread of modeled and observed values overlapped with each other. The NMB, RMSE, and *r* for monthly mean CH_2Cl_2 data against all ground measurement data are 2%, 8 ppt, and 0.95, respectively. It should be noted that over the SH regions, the model minimum and maximum values are delayed (by about 1 month) for CH_2Cl_2 compared to the measurements, while the model more accurately predicts the timing of the maximum and minimum values of C_2Cl_4. This delay difference can be explained by different source regions for CH_2Cl_2 and C_2Cl_4. In particular, Asian emission dominate SH abundance of CH_2Cl_2, while C_2Cl_4 abundance are attributed more evenly to regions, as will be discussed in Section 3.4. For C_2Cl_4, the model captured the maximum values in the high-latitude Arctic region. In the northern mid-latitudes, a less pronounced seasonal variability was observed, which was captured by the model, despite being always biased high and with a larger standard deviation. Similar to CH_2Cl_2, the model is biased low for C_2Cl_4 in the tropics and Southern Hemisphere. The NMB, RMSE, and *r* of 45%, 2 ppt, and 0.79, respectively, show the overestimation of C_2Cl_4. This is in contrast with the model being biased low, in general, against ATom data as mentioned above (NMB of −7%). The overestimation during all the months over the NH mid-latitudes and strong underestimation in the SH (i.e., emission sources) suggests either C_2Cl_4 emission magnitudes or global distributions require further improvements.

3.4. Impact of Transport and Convection From Regionally Tagged Emissions of Cl-VSLS

As shown in the previous sections, the model was mostly able to capture the distribution and seasonal variability of four Cl-VSLS. We also observed the presence of these Cl-VSLS in the SH remote regions and high altitudes despite the fact that the large majority of their emissions are in the NH. In this section, we use the regional tagged tracers (described in Section 2.2.2) to estimate the contribution of emissions from each region on Cl-VSLS abundance at various altitudes and locations.

Figure 7 shows the spatial distribution of each regional tagged CH_2Cl_2 tracer at 950 hPa and 150 hPa during August 2017. The deep convection during August 2017 due to the Asian summer monsoon (ASM) has been previously shown (Honomichl & Pan, 2020). Near the surface (i.e., 950 hPa), the highest mixing ratios are near the source regions for the Asian (AS) and European (EU) tagged tracers. The AS emissions are also the major contributor to the CH_2Cl_2 mixing ratios over North America, South America, and Africa. Similarly, the AS emissions are the dominant source of CH_2Cl_2 over the remote regions from the Arctic to the Antarctic (Figure 7a). In addition, the NH mixing ratios over the high latitude regions that are contributed by the AS region are larger than the mid-latitude regions. At high altitudes (i.e., 150 hPa), the AS emissions are the dominant contributor around the globe (Figure 7e). In particular, AS mixing ratios above 50 ppt were modeled over their source regions in contrast with <9 ppt mixing ratios from EU. Furthermore, the model shows larger values at high altitudes than at the surface in the tropics and subtropical regions in SH (Figure 7e). Figure 8, on the other hand, shows that AS, EU, and NA emissions are the dominant contributors of C_2Cl_4 in their source regions and their impact on other regions in the NH, near the surface, are within the same order. However, their contribution in the SH is minimal compared to the cumulative impact of sources in the SH (Figure 8d). At high altitudes, Asia is the dominant contributor to C_2Cl_4, and its impact is primarily limited to the tropical regions. Adcock et al. (2021) and Lauther et al. (2022) showed that the ASM anticyclone transports large amounts of surface Cl-VSLS emissions to the UTLS region, where they can be transported horizontally by jet streams to other regions.

Figures 9 and 10 show the annual zonal means of the total and tagged emissions of CH_2Cl_2 and C_2Cl_4, respectively, between 2016 and 2018. For CH_2Cl_2, we estimate the annual mean tropospheric mixing ratios of 36.9 ppt (i.e., 73.8 ppt Cl), with the Asian emissions being responsible for 85% of the total. Within Asia, we further calculated that China's annual mean tropospheric mixing ratio of CH_2Cl_2 is 17.1 ppt, which accounts for 46% of global tropospheric mean abundance. On continental scale, EU (8%) and NA (4%) emissions ranked second and third as sources of tropospheric CH_2Cl_2, respectively. Table 3 shows the mean tropospheric values in individual latitude bins, highlighting that AS emissions dominate in all regions. Similarly, the vertical profiles of tagged emissions along the ATom flight tracks confirm the AS dominance (Figure S8 in Supporting Information S1). For C_2Cl_4, in contrast, emissions from EU, NA, and AS are all important contributors to the global annual mean tropospheric mixing ratio of 0.73 ppt (i.e., 2.92 ppt Cl). The modeling results show that total chlorine from CH_2Cl_2 is ≈25 times more than from C_2Cl_4 in the troposphere. The similar source gas ratio for TOGA measurements along the ATom flight tracks is ≈28 (using 46.6 and 0.84 ppt global means of CH_2Cl_2 and C_2Cl_4, respectively, in Section 3.1.5).

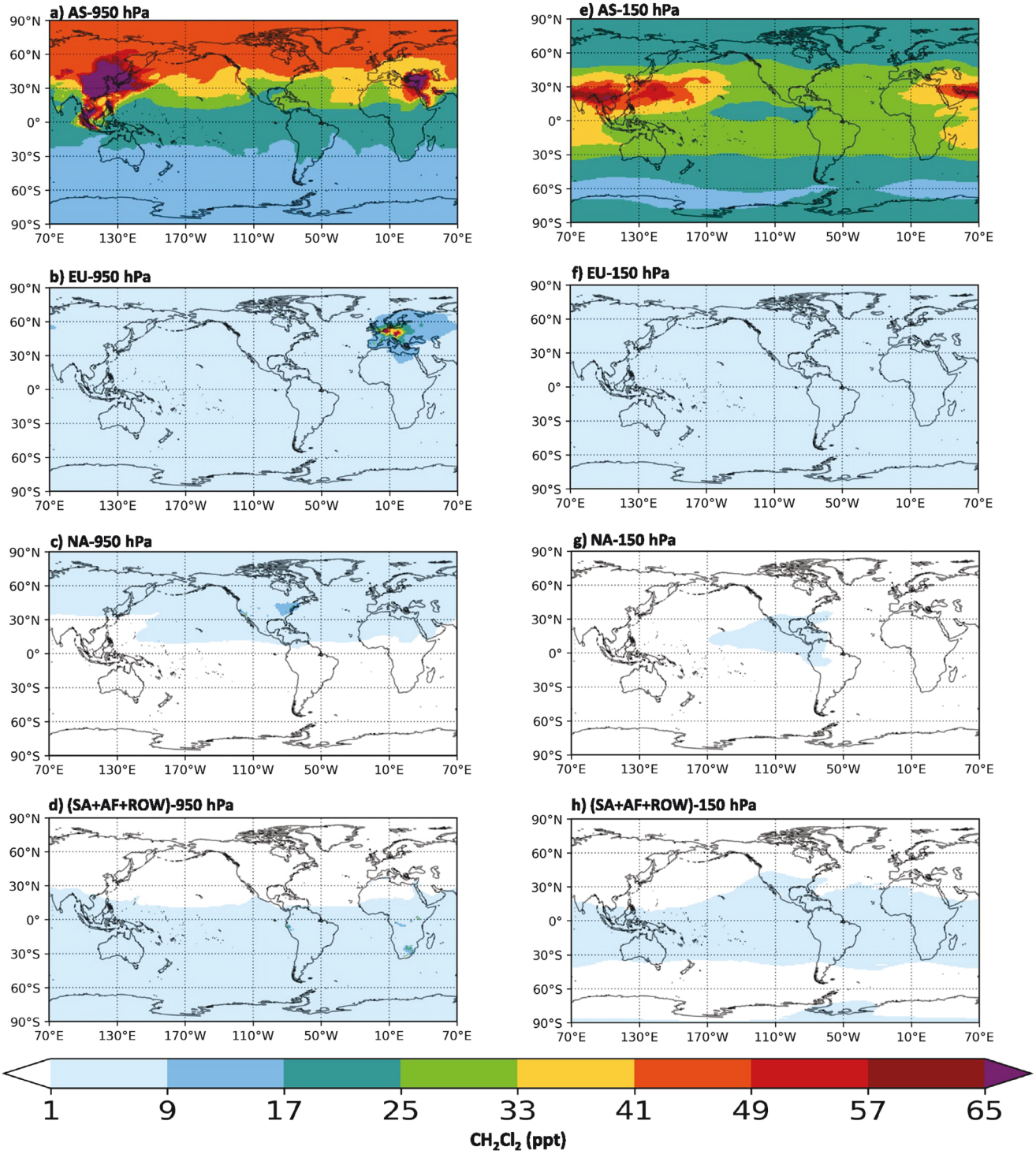

Figure 7. Maps of August 2017 mean CH_2Cl_2 mixing ratios of tagged emissions near the surface (950 hPa) and UTLS (150 hPa ≈ 13 km). AS: Asia, EU: Europe, NA: North America, SA: South America, AF: Africa, and ROW: Rest of the world.

EU, NA, and AS contribute 32% (0.23 ppt), 27% (0.20 ppt), and 33% (0.24 ppt) to the global mean C_2Cl_4, respectively. As Figure 10 shows, the C_2Cl_4 mixing ratios are highest over their individual source regions with very low values in other regions, due to its shorter atmospheric lifetime, which we will discuss in Section 3.5. While AF and SA C_2Cl_4 emissions do not strongly impact global concentrations, the tagged zonal plots shows clear sensitivity of the C_2Cl_4 distribution to regional sources. In particular, Figure 10 suggests that an increase in future AF

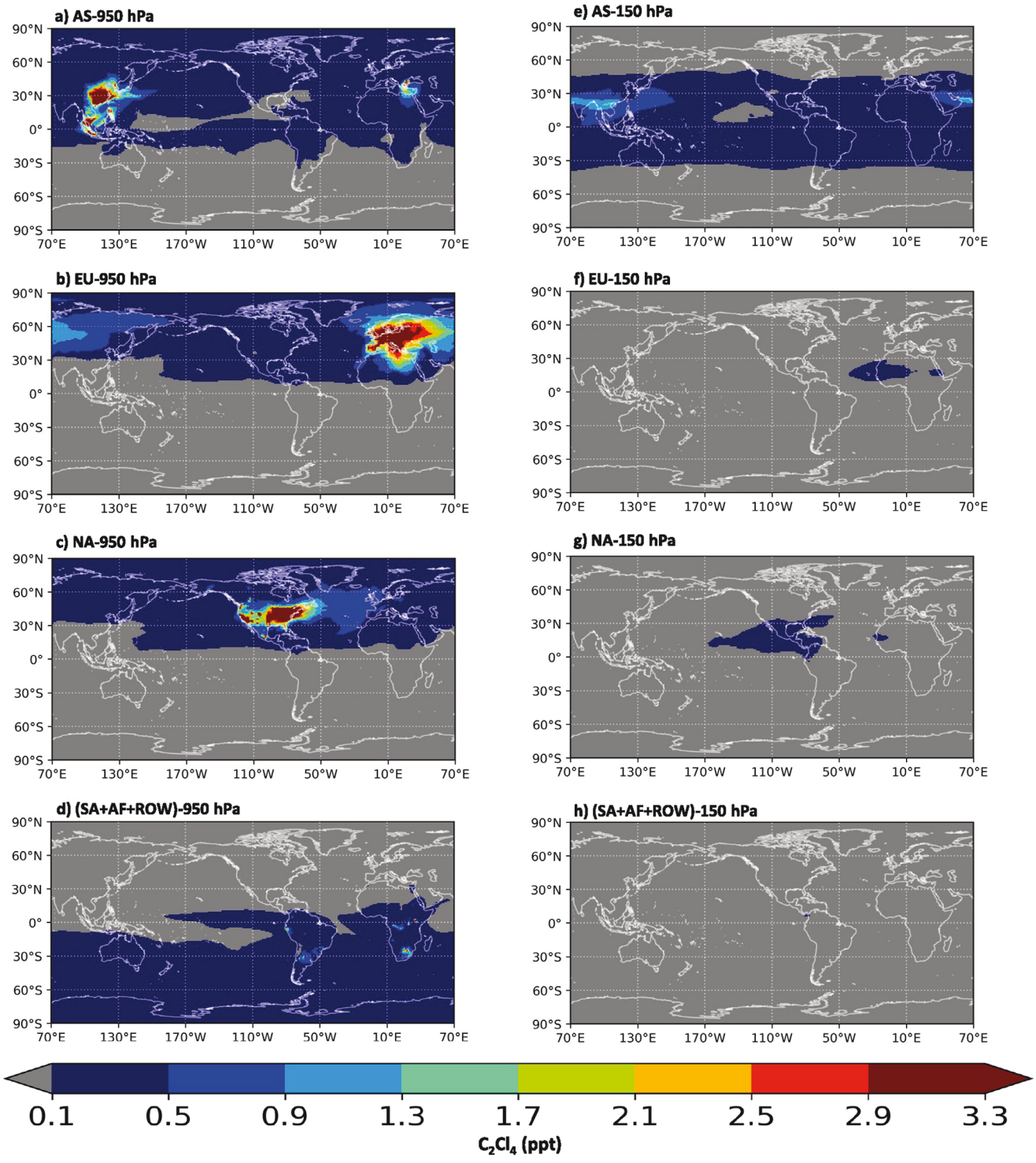

Figure 8. Same as Figure 7, but for C_2Cl_4. Note that all the values in (h) are below 0.1 ppt.

and SA emissions could have a more significant impact than other continental sources on the SH region, although an increase in C_2Cl_4 emissions is not anticipated based on current emission and concentration trends (Claxton et al., 2020; Laube et al., 2022). Figures 9 and 10 also show contributions from SA and AF over the tropics, and highlights the significance of the emission regions. This is important as these regions become increasingly industrialized. This could lead to more widespread use of VSLS in the future, which could be transported to the

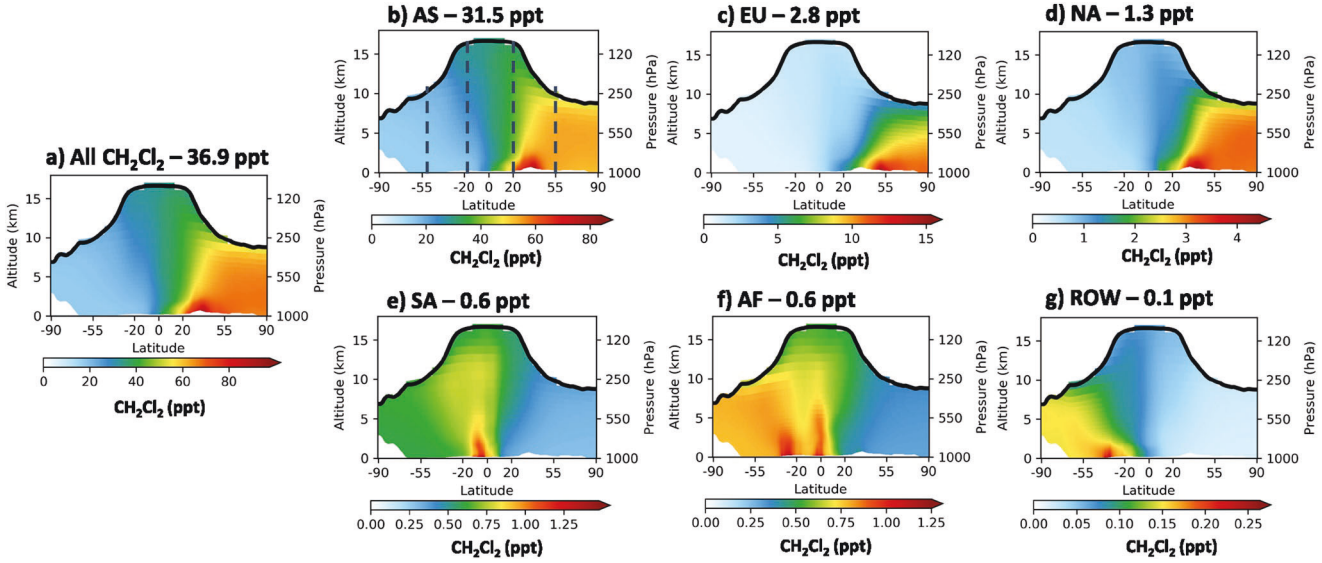

Figure 9. Modeled zonal 2016–2018 annual mean mixing ratios of (a) CH_2Cl_2 and (b–g) zonal mixing ratios resulting from tagged CH_2Cl_2 emissions from each designated region. The solid line shows the location of the mean modeled tropopause. The global tropospheric mean mixing ratios of the (a) global and (b–g) regionally sourced CH_2Cl_2 are shown on top of each panel, where AS: Asia, EU: Europe, NA: North America, SA: South America, AF: Africa, and ROW: Rest of the world. The dashed line on (b) shows the latitudinal bins used in Table 3. Note that the color scales are different in each panel.

stratosphere and impact the stratospheric ozone layer (Oram et al., 2017). The tagged emissions along the ATom flight tracks for C_2Cl_4 also show relatively higher contribution of AF and SA emissions in the SH (Figure S9 in Supporting Information S1).

3.5. Modeled Major Photochemical Destruction Pathways for Cl-VSLS

Reactions with the OH radical, Cl atoms, and photolysis are known photochemical destruction pathways of Cl-VSLS in the atmosphere and are included in the model (R1–R12). Figure 11 shows the mean rate of CH_2Cl_2 and C_2Cl_4 destruction via these reactions in different latitude bins between 2016 and 2018. For CH_2Cl_2, reaction with OH is the dominant destruction pathway in all latitude bins and within the vertical profile. Specifically, the OH reaction rate is 0.9–1.3 orders of magnitude higher than the Cl reaction rate. In addition, photolysis plays

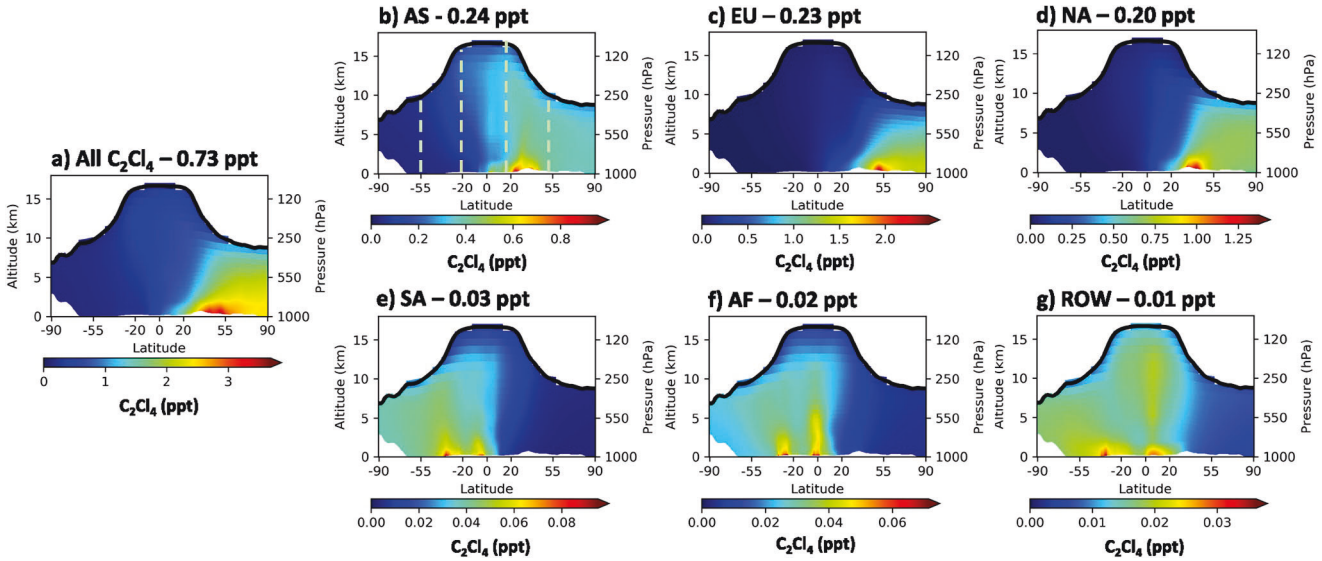

Figure 10. Same as Figure 9, but for C_2Cl_4.

Table 3
The Annual Mean (2016–2018) Modeled Tropospheric Source Contribution of CH_2Cl_2 and C_2Cl_4, in ppt, Due To Tagged Emissions in Each Source Region

Species	Region	Asia (China)	Europe	North America	South America	Africa	Rest of the world
CH_2Cl_2	High latitudes/Arctic	52.90 (31.95)	7.98	2.92	0.32	0.33	0.02
	Northern mid-latitudes	46.69 (28.39)	4.33	2.05	0.41	0.42	0.03
	Tropics	28.86 (14.13)	1.86	1.02	0.71	0.65	0.06
	Southern mid-latitudes	18.38 (8.41)	1.16	0.65	0.69	0.76	0.11
	Southern Ocean/Antarctic	14.74 (6.74)	0.96	0.54	0.62	0.78	0.14
C_2Cl_4	High latitudes/Arctic	0.36 (0.20)	0.94	0.62	0.004	0.005	0.007
	Northern mid-latitudes	0.39 (0.23)	0.42	0.40	0.01	0.01	0.01
	Tropics	0.26 (0.09)	0.10	0.11	0.03	0.03	0.02
	Southern mid-latitudes	0.10 (0.03)	0.03	0.03	0.04	0.03	0.02
	Southern Ocean/Antarctic	0.05 (0.01)	0.02	0.02	0.04	0.02	0.02

a significant role only during summer and at high altitudes. Specifically, over the SH mid-latitudes and in the tropics, the mixing ratios of CH_2Cl_2 and C_2Cl_4 decrease at a faster rate with increasing altitude (sharper gradient) when photolysis (blue line) begins to compete with the Cl reaction.

As was shown in Figure 2, the model underestimates CH_2Cl_2 mixing ratios. Reaction with OH is the main destruction process of CH_2Cl_2. As OH is calculated online in the model, it is challenging to separate the drivers of the sources and sinks of OH, thus the methane lifetime is a good indicator of the average OH concentration. In our base simulation, the lifetime of methane was 8.4 years, which is close to the reported values by other studies using CESM1 model (Nicely et al., 2020; Tilmes et al., 2015, 2016), but lower than observational estimates (Prather et al., 2012). Our model includes halogen chemistry, which has shown to increase the methane lifetime by 6%–9% (Li et al., 2022). Therefore, the uncertainties in the modeled OH (Stevenson et al., 2020) could explain the bias in part for CH_2Cl_2. To investigate the OH sensitivity of the model without directly attempting to change the OH amounts, we ran a simulation in which we reduced the rate constant k_{OH} for all four Cl-VSLS (i.e., R2, R5, R8, and R11) by 10%, which decreased the model bias for CH_2Cl_2 by 7% (Figure S10 in Supporting Information S1). It is shown that the modeled OH is not more than ∼10% too high (Stevenson et al., 2020), indicating the Cl-VSLS emissions inventories are likely too low based on the persistent bias with the adjusted OH rate constants. On the other hand, $CHCl_3$ and 1,2-DCA mixing ratios, which are based on LBC rather than emissions in our model—see Section 2.2— are not sensitive to this 10% OH perturbation experiment. It shows that further work is required to update the LBC values in the model or to develop global emission inventories for $CHCl_3$ and 1,2-DCA.

For C_2Cl_4, the OH reaction is the major destruction pathway within the lower troposphere except at high latitudes. As a result, the model NMB reduced by 5% in the OH perturbation experiment (Figure S10 in Supporting Information S1). However, the role of Cl oxidation relative to OH is substantially larger than for CH_2Cl_2 in the model. In the Arctic, there is a competition between OH and Cl oxidation pathways while the Cl reaction prevails in the Antarctic region. In other latitude bins, the Cl reaction is also found to be a dominant pathway in the free troposphere and UTLS region, in good agreement with the model study of Hossaini et al. (2019)—see their Figure 2. The photolysis reaction is not an important photochemical destruction pathway in the lower troposphere for C_2Cl_4 either. However, photolysis of C_2Cl_4 becomes influential in the UTLS region.

Figure 2 showed that modeled C_2Cl_4 was too low in the upper troposphere of the NH mid-latitude region. Our k_{OH} perturbation experiment (Figure S10 in Supporting Information S1) shows an infinitesimal improvement for C_2Cl_4, indicating the Cl reaction as its main destruction pathway. The Cl reaction being the dominant pathway in high altitudes requires the presence of Cl atoms in the model. Inorganic chlorine species are the main sources of Cl atoms in the troposphere (Wang, Jacob, et al., 2019). Our results suggest photolysis of molecular chlorine (Cl_2), formed due to acid displacement and heterogeneous reactions (Li et al., 2022) including stoichiometric ice recycling in the UT (Fernandez et al., 2014), as the potential source of Cl atoms in high latitudes in the model (Figure S11 in Supporting Information S1). However, ATom measurements made by the NOAA chemical ionization mass spectrometer (CIMS) instrument show a different spatial distribution (and mean abundance) of Cl_2 with higher mixing ratios in the tropics and subtropical lower troposphere (Figure S12 in Supporting Information S1).

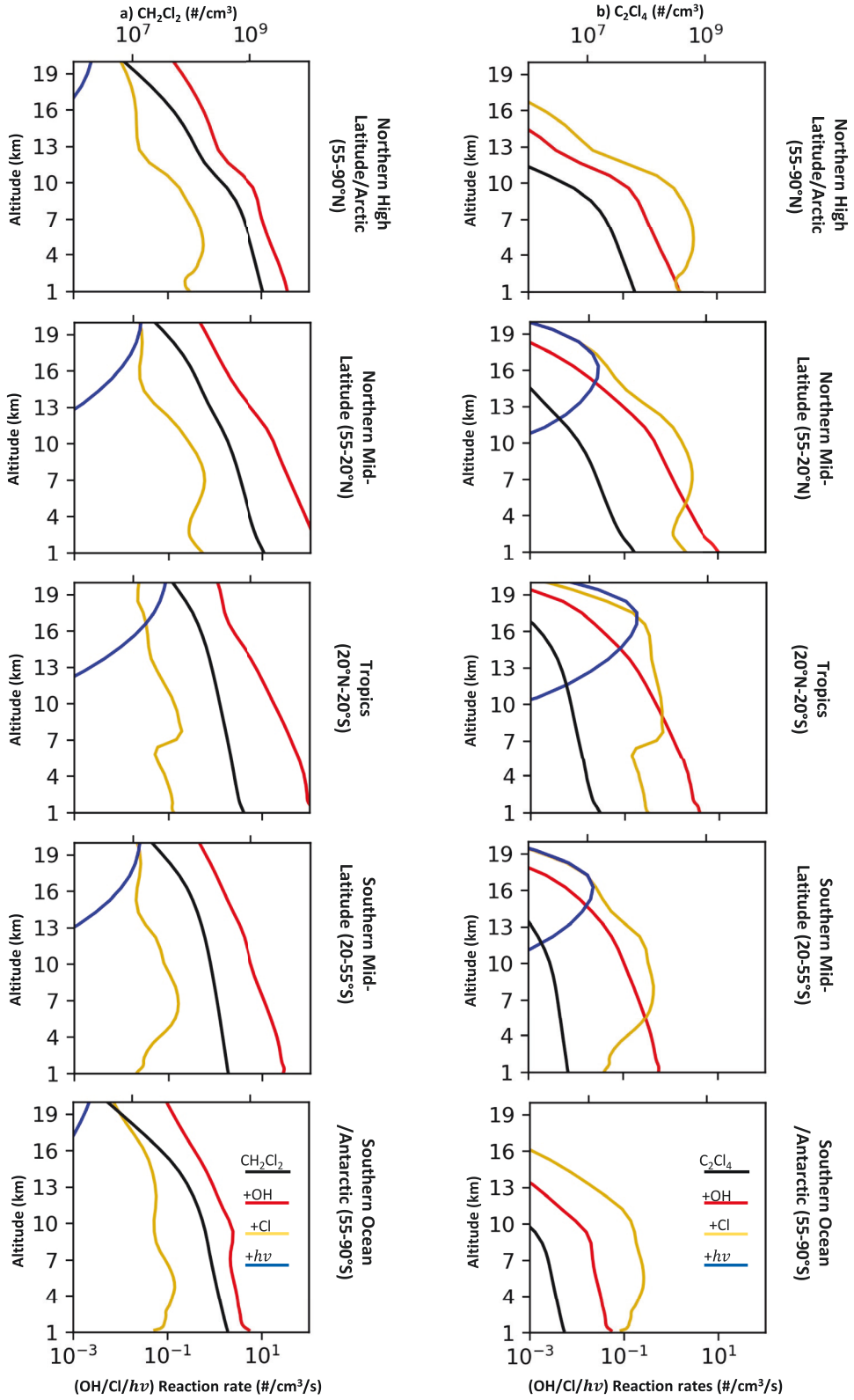

Figure 11. Vertical profiles of 2016–2018 annual mean modeled mixing ratios (black; top *x*-axis) and reaction rates (colors; bottom *x*-axis) for CH_2Cl_2 (left column) and C_2Cl_4 (right column) over five latitude bins around the world (not only along ATom flight tracks—see text). Note that *x*-axes are in logarithmic scale.

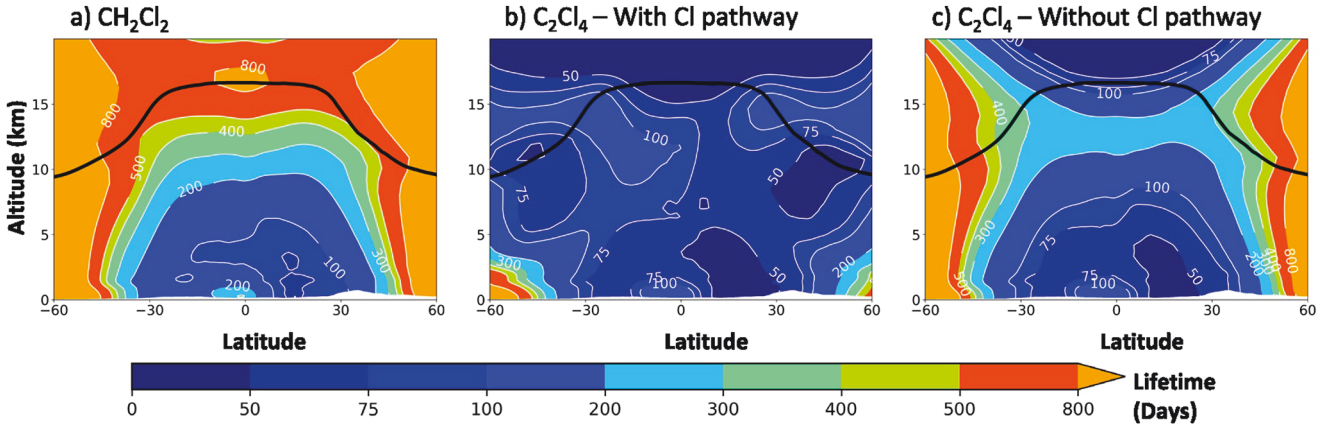

Figure 12. Modeled zonal 2016–2018 annual mean local lifetimes of (a) CH_2Cl_2 and (b, c) C_2Cl_4. Panel (b) shows the C_2Cl_4 local lifetime based on all the reactions (OH, Cl, and $h\nu$) while (c) includes only OH reaction and photolysis (i.e., without Cl pathway). The solid line shows the mean tropopause location.

Also, the larger bias of modeled C_2Cl_4 in high altitudes over the mid-latitude region during the ATom mission does not support the modeled dominant contribution through reactions with Cl atoms (Figure 2). On the other hand, the source of active chlorine in the atmosphere has still large uncertainties (Wang et al., 2021). Thus, we are investigating our model bias for Cl_2 but have not resolved this.

Current emission estimates suggest that anthropogenic C_2Cl_4 emissions are about 10 times lower than CH_2Cl_2 (Claxton et al., 2020). However, the NH low-altitude (<4 km or θ < 320 K) measured C_2Cl_4 to CH_2Cl_2 ratio is 0.02 during the ATom mission, which is consistent with the shorter lifetime of C_2Cl_4 (Hossaini et al., 2019). Figure 12 shows the local lifetime of CH_2Cl_2 and C_2Cl_4 averaged between 2016 and 2018, calculated based on their partial destruction reaction rates. Overall, the CH_2Cl_2 lifetime increases when moving from tropics toward the mid-latitudes and higher altitudes, from ∼75 days over the tropical boundary layer up to ∼500 days around the tropical tropopause. In addition, the CH_2Cl_2 local lifetime has a seasonal variation (Figure S13 in Supporting Information S1): it is shorter in the NH during warmer seasons (e.g., JJA) than colder seasons (e.g., DJF). Nevertheless, the shortest boundary layer CH_2Cl_2 local lifetime is always predicted to be over the NH mid-latitudes (Figure S13 in Supporting Information S1).

The local lifetime of C_2Cl_4 is shorter than CH_2Cl_2, ranging between ∼50 days in the tropical boundary layer to ∼100 days near the tropical tropopause. This is primarily due to the strong oxidation rate of C_2Cl_4 with Cl atoms in our model as discussed above. Figure 12 also shows the C_2Cl_4 local lifetime without considering the Cl destruction pathway, which resembles more to the shape of CH_2Cl_2 local lifetime plots. Regardless, C_2Cl_4 without the Cl destruction pathway still has a shorter lifetime than CH_2Cl_2 in the UTLS region. The shorter lifetime (and more chlorine atoms per molecule) of C_2Cl_4 in the UTLS region suggests that in a case of deep convection, on a molecule/molecule basis, C_2Cl_4 more rapidly liberates its Cl in the UTLS compared to CH_2Cl_2.

4. Summary and Conclusions

In this study, measurements of four Cl-VSLS from surface and aircraft-based programs are compared to the CESM model that includes updated chlorine chemistry. The bulk of the analyses focus on ATom data, which provided geographical coverage throughout the Pacific and Atlantic troposphere and nearly pole-to-pole. The detailed emission inventories for CH_2Cl_2 and C_2Cl_4 by Claxton et al. (2020) are used in the model. The $CHCl_3$ is prescribed as surface boundary condition (vs. emissions) as it is largely emitted by natural sources, and its emissions are less well known although recent studies have tried to constrain its growing anthropogenic emissions (An et al., 2023; Fang et al., 2019). Similarly, 1,2-dichloroethane (1,2-DCA) is prescribed as surface boundary conditions as its emissions are even less well known than $CHCl_3$.

Aircraft-based measurement data from the NCAR TOGA, UCI WAS and NOAA PFP instruments are presented and compared. The agreement between the measurements is reasonably good and generally within reported uncertainties, but some significant differences exist, which have not yet been resolved. For example, a fairly large

discrepancy (up to 60% = 17 ppt for CH_2Cl_2) in the high altitudes of the Southern Ocean and Antarctic region during ATom-3 and ATom-4.

The bulk of the model-measurement comparisons were made using the NCAR TOGA data for which there is the greatest spatial coverage. Detailed comparisons are presented for CH_2Cl_2 and C_2Cl_4. The model does a reasonable job of simulating the vertical profiles of all four Cl-VSLS species. However, the model generally underestimated the mixing ratios of CH_2Cl_2, most significantly in the northern mid-latitudes and tropics; it also generally underestimated C_2Cl_4, particularly in the tropics and southern latitudes. The model comparisons with surface observations from AGAGE and NOAA networks indicate a reasonable representation of the Cl-VSLS mole fraction seasonal cycles in the model, with the global mean being biased low and high for CH_2Cl_2 and C_2Cl_4, respectively. These biases primarily point to uncertainties in the emissions, in terms of both magnitudes and global distribution.

Measurement profiles over the northern mid-latitudes show a large enhancement of CH_2Cl_2 mixing ratios over the Pacific Ocean compared to the Atlantic Ocean. We attribute this to the Pacific being closer to the largest source region for this species and the lifetime of the species of approximately 4 months, which precludes uniform hemispheric mixing. This is consistent with our analysis of the regionally tagged CH_2Cl_2 emissions. C_2Cl_4 and $CHCl_3$ also showed general enhancements for the Pacific versus Atlantic Ocean. In the NH, Cl-VSLS have sources that are generally co-located and strong correlations between them were noted. The correlations break down in the SH because $CHCl_3$ sources in the SH have a significant natural component whereas CH_2Cl_2 and C_2Cl_4 do not (Feng et al., 2018; Worton et al., 2006). Significant NH/SH gradients were observed for CH_2Cl_2 and C_2Cl_4 (and $CHCl_3$ and 1,2-DCA) owing to their source locations and lifetimes with respect to interhemispheric mixing. This was a good test for the model oxidation rates and transport capability and showed that the model simulated the inter-hemispheric distribution of these Cl-VSLS quite well.

To further investigate how Cl-VSLS are redistributed globally after release from their sources, we separated the globe into specific regions, and "tagged" model emissions for CH_2Cl_2 and C_2Cl_4 from each of these regions and investigated their global distribution. The annual zonal means of the tagged emissions showed that Asian emissions (AS) dominate the global distributions of these species both near the surface (950 hPa) and at high altitudes (150 hPa), representing up to 70% of the annual mean tropospheric mixing ratios of 36.9 ppt CH_2Cl_2 (73.8 ppt Cl). For C_2Cl_4, EU, NA, and AS are all important contributors to the global annual mean modeled tropospheric mixing ratios of 0.73 ppt (2.92 ppt Cl). Therefore, the contribution of source gas CH_2Cl_2 to the global Cl^{VSLS} burden is approximately 25 times larger than that arising from C_2Cl_4 based on the modeling results averaged between 2016 and 2018. Similar calculations using NCAR TOGA data, along the ATom flight tracks, led to a factor of ≈28 (using global mean observed mixing ratios of 46.6 and 0.84 ppt for CH_2Cl_2 and C_2Cl_4, respectively).

Finally, we investigate the primary loss pathways for CH_2Cl_2 and C_2Cl_4 as a function of altitude and latitude within the model framework and we find that reaction with OH dominates the loss rate of CH_2Cl_2 at all latitudes and altitudes while photolysis plays only a minor role and only at high altitudes. For C_2Cl_4, the reaction with OH represents the most significant loss process, but given the Cl abundances calculated in the model, the reaction with chlorine atoms is competitive with OH in the mid-troposphere and UTLS region, while photolysis is a significant loss process in the LS. This conclusion hinges on the accuracy of the Cl calculated in the model, and further analysis is required to determine if the Cl loss pathway is overestimated in the model given ATom observations of high concentrations of Cl_2 in the remote troposphere and the new Cl atom formation mechanism proposed by van Herpen et al. (2023).

In summary, the data sets reported here have provided the best global data coverage to date for Cl-VSLS species and have provided us with the opportunity to test our understanding of global distributions by comparing the measurements with model simulations. The model provided insights into global distributions and pathways. Overall, the model did a reasonable job but missed some observed features such as enhanced low-altitude concentrations of Cl-VSLS (potentially due to both magnitudes and distribution of emissions) and Cl_2 concentrations in the free troposphere that require further study. In our future work, we will study the impact of global atmospheric circulation phenomena such as Asian Summer Monsoon Anticyclone and the North American Monsoon Anticyclone as fast transport pathways of VSLS to the UTLS region, by utilizing the data measured during the 2022 Asian Summer Monsoon Chemical and Climate Impact Project (ACCLIP) and 2021–2022 Dynamics and Chemistry of the Summer Stratosphere (DCOTSS) missions, respectively.

Conflict of Interest

The authors declare no conflicts of interest relevant to this study.

Data Availability Statement

CAM-chem is a component of the NCAR CESM which is publicly available on the project website (http://www.cesm.ucar.edu/). The NCAR TOGA, UCI WAS, NOAA PFP, NOAA CIMS, and ATHOS chemical composition data, and NASA DC-8 positional and meteorological measurements for the NASA ATom campaign are available from Wofsy et al. (2021). The ORCAS and CONTRAST data are publicly available from Apel (2017) and Apel and Hornbrook (2014), respectively. The NOAA ground-based measurements were supported in part by NOAA's Atmospheric Chemistry, Carbon Cycle and Climate Program of its Climate Program Office and are available from https://gml.noaa.gov/hats/data.html and https://gml.noaa.gov/aftp/data/hats/solvents/. Data from the AGAGE monitoring network are available from https://agage.mit.edu/data/. The model results used in this study are available from Zenodo data repository (https://doi.org/10.5281/zenodo.10021453, Roozitalab et al., 2023).

Acknowledgments

This work is supported by the National Science Foundation (NSF) through its funding of the National Center for Atmospheric Research (NCAR), under cooperative agreement number 1852977. Specific funding was provided by NSF award #2032328. This research was enabled by the computational and storage resources of NCAR's Computational and Information Systems Laboratory (CISL), sponsored by the NSF. Cheyenne: HPE/SGI ICE XA System (NCAR Community Computing). Boulder, CO: National Center for Atmospheric Research. https://doi.org/10.5065/D6RX99HX. This research was also funded in part by NASA Award No. NNX15AG69A. We thank the international AGAGE science team for making their data available, and acknowledge that the 7 stations used in this paper are supported principally by multiple NASA (USA) grants to Massachusetts Institute of Technology (with sub-awards to Bristol University, and Commonwealth Scientific and Industrial Research Organisation (CSIRO) and to Scripps Institution of Oceanography (SIO, including central AGAGE calibration). Support also comes from: Department of Business, Energy, and Industrial Strategy (UK) and NOAA (USA) grants to Bristol University; CSIRO and Bureau of Meteorology (Australia); Federal Office for the Environment (FOEN) grants to Swiss Federal Laboratories for Materials Science and Technology (Switzerland; and by Norwegian Institute for Air Research (Norway). NOAA's PFP measurements were facilitated by F. Moore, K. McKain, C. Siso, B. Miller, B. Hall, and J. Elkins.

References

Adcock, K. E., Fraser, P. J., Hall, B. D., Langenfelds, R. L., Lee, G., Montzka, S. A., et al. (2021). Aircraft-based observations of ozone-depleting substances in the upper troposphere and lower stratosphere in and above the Asian summer monsoon. *Journal of Geophysical Research: Atmospheres*, *126*(1), e2020JD033137. https://doi.org/10.1029/2020JD033137

An, M., Western, L. M., Hu, J., Yao, B., Mühle, J., Ganesan, A. L., et al. (2023). Anthropogenic chloroform emissions from China drive changes in global emissions. *Environmental Science & Technology*, *57*(37), 13925–13936. https://doi.org/10.1021/acs.est.3c01898

An, M., Western, L. M., Say, D., Chen, L., Claxton, T., Ganesan, A. L., et al. (2021). Rapid increase in dichloromethane emissions from China inferred through atmospheric observations. *Nature Communications*, *12*(1), 7279. https://doi.org/10.1038/s41467-021-27592-y

Andrews, S. J., Carpenter, L. J., Apel, E. C., Atlas, E., Donets, V., Hopkins, J. R., et al. (2016). A comparison of very short lived halocarbon (VSLS) and DMS aircraft measurements in the tropical west Pacific from CAST, ATTREX and CONTRAST. *Atmospheric Measurement Techniques*, *9*(10), 5213–5225. https://doi.org/10.5194/amt-9-5213-2016

Apel, E. C. (2017). ORCAS trace organic gas analyzer (TOGA) VOC data version 1.0. https://doi.org/10.5065/D6639N5B

Apel, E. C., & Hornbrook, R. S. (2014). *NSF/NCAR GV HIAPER TOGA VOC analyzer data. Version 1.0*. UCAR/NCAR—Earth Observing Laboratory. https://doi.org/10.5065/D6NG4P0F

Apel, E. C., Hornbrook, R. S., Hills, A. J., Blake, N. J., Barth, M. C., Weinheimer, A., et al. (2015). Upper tropospheric ozone production from lightning NO_x-impacted convection: Smoke ingestion case study from the DC3 campaign. *Journal of Geophysical Research: Atmospheres*, *120*(6), 2505–2523. https://doi.org/10.1002/2014JD022121

Butler, R., Palmer, P. I., Feng, L., Andrews, S. J., Atlas, E. L., Carpenter, L. J., et al. (2018). Quantifying the vertical transport of $CHBr_3$ and CH_2Br_2 over the western Pacific. *Atmospheric Chemistry and Physics*, *18*(17), 13135–13153. https://doi.org/10.5194/acp-18-13135-2018

Carpenter, L. J., & Liss, P. S. (2000). On temperate sources of bromoform and other reactive organic bromine gases. *Journal of Geophysical Research*, *105*(D16), 20539–20547. https://doi.org/10.1029/2000JD900242

Chipperfield, M. P., Dhomse, S., Hossaini, R., Feng, W., Santee, M. L., Weber, M., et al. (2018). On the cause of recent variations in lower stratospheric ozone. *Geophysical Research Letters*, *45*(11), 5718–5726. https://doi.org/10.1029/2018GL078071

Chipperfield, M. P., Hossaini, R., Montzka, S. A., Reimann, S., Sherry, D., & Tegtmeier, S. (2020). Renewed and emerging concerns over the production and emission of ozone-depleting substances. *Nature Reviews Earth & Environment*, *1*(5), 251–263. https://doi.org/10.1038/s43017-020-0048-8

Claxton, T., Hossaini, R., Wilson, C., Montzka, S. A., Chipperfield, M. P., Wild, O., et al. (2020). A synthesis inversion to constrain global emissions of two very short lived chlorocarbons: Dichloromethane, and perchloroethylene. *Journal of Geophysical Research: Atmospheres*, *125*(12), e2019JD031818. https://doi.org/10.1029/2019JD031818

Daniel, J. S., Solomon, S., Portmann, R. W., & Garcia, R. R. (1999). Stratospheric ozone destruction: The importance of bromine relative to chlorine. *Journal of Geophysical Research*, *104*(D19), 23871–23880. https://doi.org/10.1029/1999JD900381

Deming, B. L., Pagonis, D., Liu, X., Day, D. A., Talukdar, R., Krechmer, J. E., et al. (2019). Measurements of delays of gas-phase compounds in a wide variety of tubing materials due to gas–wall interactions. *Atmospheric Measurement Techniques*, *12*(6), 3453–3461. https://doi.org/10.5194/amt-12-3453-2019

Dhomse, S. S., Feng, W., Montzka, S. A., Hossaini, R., Keeble, J., Pyle, J. A., et al. (2019). Delay in recovery of the Antarctic ozone hole from unexpected CFC-11 emissions. *Nature Communications*, *10*(1), 5781. https://doi.org/10.1038/s41467-019-13717-x

Emmons, L. K., Hess, P. G., Lamarque, J. F., & Pfister, G. G. (2012). Tagged ozone mechanism for MOZART-4, CAM-chem and other chemical transport models. *Geoscientific Model Development*, *5*(6), 1531–1542. https://doi.org/10.5194/gmd-5-1531-2012

Emmons, L. K., Walters, S., Hess, P. G., Lamarque, J. F., Pfister, G. G., Fillmore, D., et al. (2010). Description and evaluation of the model for ozone and related chemical tracers, version 4 (MOZART-4). *Geoscientific Model Development*, *3*(1), 43–67. https://doi.org/10.5194/gmd-3-43-2010

Engel, A., Rigby, M., Burkholder, J. B., Fernandez, R. P., Froidevaux, L., Hall, B. D., et al. (2018). Update on ozone-depleting substances (ODSs) and other gases of interest to the Montreal protocol, chapter 1 in scientific assessment of ozone depletion. In *Global ozone research and monitoring project—Report No. 58*.

Fang, X., Park, S., Saito, T., Tunnicliffe, R., Ganesan, A. L., Rigby, M., et al. (2019). Rapid increase in ozone-depleting chloroform emissions from China. *Nature Geoscience*, *12*(2), 89–93. https://doi.org/10.1038/s41561-018-0278-2

Feng, Y., Bie, P., Wang, Z., Wang, L., & Zhang, J. (2018). Bottom-up anthropogenic dichloromethane emission estimates from China for the period 2005–2016 and predictions of future emissions. *Atmospheric Environment*, *186*, 241–247. https://doi.org/10.1016/j.atmosenv.2018.05.039

Fernandez, R. P., Salawitch, R. J., Kinnison, D. E., Lamarque, J. F., & Saiz-Lopez, A. (2014). Bromine partitioning in the tropical tropopause layer: Implications for stratospheric injection. *Atmospheric Chemistry and Physics*, *14*(24), 13391–13410. https://doi.org/10.5194/acp-14-13391-2014

Gelaro, R., McCarty, W., Suárez, M. J., Todling, R., Molod, A., Takacs, L., et al. (2017). The Modern-Era Retrospective Analysis for Research and Applications, Version 2 (MERRA-2). *Journal of Climate*, *30*(14), 5419–5454. https://doi.org/10.1175/JCLI-D-16-0758.1

Granier, C., Darras, S., van Der Gon, H. D., Jana, D., Elguindi, N., Bo, G., et al. (2019). The Copernicus atmosphere monitoring service global and regional emissions (April 2019 version).

Guenther, A. B., Jiang, X., Heald, C. L., Sakulyanontvittaya, T., Duhl, T., Emmons, L. K., & Wang, X. (2012). The model of emissions of gases and aerosols from nature version 2.1 (MEGAN2.1): An extended and updated framework for modeling biogenic emissions. *Geoscientific Model Development*, *5*(6), 1471–1492. https://doi.org/10.5194/gmd-5-1471-2012

Harris, N. R. P., Carpenter, L. J., Lee, J. D., Vaughan, G., Filus, M. T., Jones, R. L., et al. (2017). Coordinated airborne studies in the tropics (CAST). *Bulletin of the American Meteorological Society*, *98*(1), 145–162. https://doi.org/10.1175/BAMS-D-14-00290.1

Hoesly, R. M., Smith, S. J., Feng, L., Klimont, Z., Janssens-Maenhout, G., Pitkanen, T., et al. (2018). Historical (1750–2014) anthropogenic emissions of reactive gases and aerosols from the Community Emissions Data System (CEDS). *Geoscientific Model Development*, *11*(1), 369–408. https://doi.org/10.5194/gmd-11-369-2018

Honomichl, S. B., & Pan, L. L. (2020). Transport from the Asian summer monsoon anticyclone over the western Pacific. *Journal of Geophysical Research: Atmospheres*, *125*(13), e2019JD032094. https://doi.org/10.1029/2019JD032094

Hossaini, R., Atlas, E., Dhomse, S. S., Chipperfield, M. P., Bernath, P. F., Fernando, A. M., et al. (2019). Recent trends in stratospheric chlorine from very short-lived substances. *Journal of Geophysical Research: Atmospheres*, *124*(4), 2318–2335. https://doi.org/10.1029/2018JD029400

Hossaini, R., Chipperfield, M. P., Montzka, S. A., Leeson, A. A., Dhomse, S. S., & Pyle, J. A. (2017). The increasing threat to stratospheric ozone from dichloromethane. *Nature Communications*, *8*(1), 15962. https://doi.org/10.1038/ncomms15962

Hossaini, R., Chipperfield, M. P., Saiz-Lopez, A., Fernandez, R., Monks, S., Feng, W., et al. (2016). A global model of tropospheric chlorine chemistry: Organic versus inorganic sources and impact on methane oxidation. *Journal of Geophysical Research: Atmospheres*, *121*(23), 14271–214297. https://doi.org/10.1002/2016JD025756

Hu, L., Montzka, S. A., Miller, J. B., Andrews, A. E., Lehman, S. J., Miller, B. R., et al. (2015). U.S. emissions of HFC-134a derived for 2008–2012 from an extensive flask-air sampling network. *Journal of Geophysical Research: Atmospheres*, *120*(2), 801–825. https://doi.org/10.1002/2014JD022617

Hurrell, J. W., Holland, M. M., Gent, P. R., Ghan, S., Kay, J. E., Kushner, P. J., et al. (2013). The Community Earth System Model: A framework for collaborative research. *Bulletin of the American Meteorological Society*, *94*(9), 1339–1360. https://doi.org/10.1175/BAMS-D-12-00121.1

Jesswein, M., Fernandez, R. P., Berná, L., Saiz-Lopez, A., Grooß, J. U., Hossaini, R., et al. (2022). Global seasonal distribution of CH_2Br_2 and $CHBr_3$ in the upper troposphere and lower stratosphere. *Atmospheric Chemistry and Physics*, *22*, 15049–15070. https://doi.org/10.5194/acp-22-15049-2022

Keber, T., Bönisch, H., Hartick, C., Hauck, M., Lefrancois, F., Obersteiner, F., et al. (2020). Bromine from short-lived source gases in the extra-tropical northern hemispheric upper troposphere and lower stratosphere (UTLS). *Atmospheric Chemistry and Physics*, *20*(7), 4105–4132. https://doi.org/10.5194/acp-20-4105-2020

Keene, W. C., Khalil, M. A. K., Erickson, D. J., III., McCulloch, A., Graedel, T. E., Lobert, J. M., et al. (1999). Composite global emissions of reactive chlorine from anthropogenic and natural sources: Reactive chlorine emissions inventory. *Journal of Geophysical Research*, *104*(D7), 8429–8440. https://doi.org/10.1029/1998JD100084

Keng, F. S.-L., Phang, S.-M., Abd Rahman, N., Yeong, H.-Y., Malin, G., Leedham Elvidge, E., & Sturges, W. (2021). Halocarbon emissions by selected tropical seaweeds exposed to different temperatures. *Phytochemistry (Elsevier)*, *190*, 112869. https://doi.org/10.1016/j.phytochem.2021.112869

Khalil, M. A. K., & Rasmussen, R. A. (1999). Atmospheric chloroform. *Atmospheric Environment*, *33*(7), 1151–1158. https://doi.org/10.1016/S1352-2310(98)00233-7

Kinnison, D. E., Brasseur, G. P., Walters, S., Garcia, R. R., Marsh, D. R., Sassi, F., et al. (2007). Sensitivity of chemical tracers to meteorological parameters in the MOZART-3 chemical transport model. *Journal of Geophysical Research*, *112*(D20), D20302. https://doi.org/10.1029/2006JD007879

Klobas, J. E., Weisenstein, D. K., Salawitch, R. J., & Wilmouth, D. M. (2020). Reformulating the bromine alpha factor and equivalent effective stratospheric chlorine (EESC): Evolution of ozone destruction rates of bromine and chlorine in future climate scenarios. *Atmospheric Chemistry and Physics*, *20*(15), 9459–9471. https://doi.org/10.5194/acp-20-9459-2020

Lamarque, J. F., Emmons, L. K., Hess, P. G., Kinnison, D. E., Tilmes, S., Vitt, F., et al. (2012). CAM-chem: Description and evaluation of interactive atmospheric chemistry in the Community Earth System Model. *Geoscientific Model Development*, *5*(2), 369–411. https://doi.org/10.5194/gmd-5-369-2012

Laturnus, F., Haselmann, K. F., Borch, T., & Grøn, C. (2002). Terrestrial natural sources of trichloromethane (chloroform, $CHCl_3$)—An overview. *Biogeochemistry*, *60*(2), 121–139. https://doi.org/10.1023/A:1019887505651

Laube, J. C., Tegtmeier, S., Fernandez, R. P., Harrison, J. J., Hu, L., Krummel, P. B., et al. (2022). Update on ozone-depleting substances (ODSs) and other gases of interest to the Montreal protocol, chapter 1 in scientific assessment of ozone depletion. In *Global ozone research and monitoring project—Report No. 278*.

Lauther, V., Vogel, B., Wintel, J., Rau, A., Hoor, P., Bense, V., et al. (2022). In situ observations of CH_2Cl_2 and $CHCl_3$ show efficient transport pathways for very short-lived species into the lower stratosphere via the Asian and the North American summer monsoon. *Atmospheric Chemistry and Physics*, *22*(3), 2049–2077. https://doi.org/10.5194/acp-22-2049-2022

Leedham Elvidge, E. C., Oram, D. E., Laube, J. C., Baker, A. K., Montzka, S. A., Humphrey, S., et al. (2015). Increasing concentrations of dichloromethane, CH_2Cl_2, inferred from CARIBIC air samples collected 1998–2012. *Atmospheric Chemistry and Physics*, *15*(4), 1939–1958. https://doi.org/10.5194/acp-15-1939-2015

Li, Q., Fernandez, R. P., Hossaini, R., Iglesias-Suarez, F., Cuevas, C. A., Apel, E. C., et al. (2022). Reactive halogens increase the global methane lifetime and radiative forcing in the 21st century. *Nature Communications*, *13*(1), 2768. https://doi.org/10.1038/s41467-022-30456-8

Neale, R., Richter, J., Park, S., Lauritzen, P., Vavrus, S., Rasch, P., & Zhang, M. (2013). The mean climate of the Community Atmosphere Model (CAM4) in forced SST and fully coupled experiments. *Journal of Climate*, *26*(14), 5150–5168. https://doi.org/10.1175/JCLI-D-12-00236.1

Nicely, J. M., Duncan, B. N., Hanisco, T. F., Wolfe, G. M., Salawitch, R. J., Deushi, M., et al. (2020). A machine learning examination of hydroxyl radical differences among model simulations for CCMI-1. *Atmospheric Chemistry and Physics*, *20*(3), 1341–1361. https://doi.org/10.5194/acp-20-1341-2020

Oelhaf, H., Sinnhuber, B.-M., Woiwode, W., Bönisch, H., Bozem, H., Engel, A., et al. (2019). POLSTRACC: Airborne experiment for studying the polar stratosphere in a changing climate with the high altitude and long range research aircraft (HALO). *Bulletin of the American Meteorological Society*, *100*, 2634–2664. https://doi.org/10.1175/BAMS-D-18-0181.1

Oram, D. E., Ashfold, M. J., Laube, J. C., Gooch, L. J., Humphrey, S., Sturges, W. T., et al. (2017). A growing threat to the ozone layer from short-lived anthropogenic chlorocarbons. *Atmospheric Chemistry and Physics*, *17*(19), 11929–11941. https://doi.org/10.5194/acp-17-11929-2017

Ordóñez, C., Lamarque, J. F., Tilmes, S., Kinnison, D. E., Atlas, E. L., Blake, D. R., et al. (2012). Bromine and iodine chemistry in a global chemistry-climate model: Description and evaluation of very short-lived oceanic sources. *Atmospheric Chemistry and Physics*, *12*(3), 1423–1447. https://doi.org/10.5194/acp-12-1423-2012

Pan, L. L., Atlas, E. L., Salawitch, R. J., Honomichl, S. B., Bresch, J. F., Randel, W. J., et al. (2017). The convective transport of active species in the tropics (CONTRAST) experiment. *Bulletin of the American Meteorological Society*, *98*(1), 106–128. https://doi.org/10.1175/BAMS-D-14-00272.1

Prather, M. J., Holmes, C. D., & Hsu, J. (2012). Reactive greenhouse gas scenarios: Systematic exploration of uncertainties and the role of atmospheric chemistry. *Geophysical Research Letters*, *39*(9), L09803. https://doi.org/10.1029/2012GL051440

Prinn, R. G., Weiss, R. F., Arduini, J., Arnold, T., DeWitt, H. L., Fraser, P. J., et al. (2018). History of chemically and radiatively important atmospheric gases from the advanced global atmospheric gases experiment (AGAGE). *Earth System Science Data*, *10*(2), 985–1018. https://doi.org/10.5194/essd-10-985-2018

Prinn, R. G., Weiss, R. F., Fraser, P. J., Simmonds, P. G., Cunnold, D. M., Alyea, F. N., et al. (2000). A history of chemically and radiatively important gases in air deduced from ALE/GAGE/AGAGE. *Journal of Geophysical Research*, *105*(D14), 17751–17792. https://doi.org/10.1029/2000JD900141

Roozitalab, B., Emmons, L. K., Hornbrook, R. S., Kinnison, D. E., Fernandez, R. P., Li, Q., et al. (2023). CESM short lived Halogen simulation results for Roozitalab et al. (2023) [Dataset]. Journal of Geophysical Research: Atmospheres, Zenodo. https://doi.org/10.5281/zenodo.10021453

Saiz-Lopez, A., Fernandez, R. P., Ordóñez, C., Kinnison, D. E., Gómez Martín, J. C., Lamarque, J. F., & Tilmes, S. (2014). Iodine chemistry in the troposphere and its effect on ozone. *Atmospheric Chemistry and Physics*, *14*(23), 13119–13143. https://doi.org/10.5194/acp-14-13119-2014

Saiz-Lopez, A., & von Glasow, R. (2012). Reactive halogen chemistry in the troposphere. *Chemical Society Reviews*, *41*(19), 6448–6472. https://doi.org/10.1039/C2CS35208G

Say, D., Ganesan, A. L., Lunt, M. F., Rigby, M., O'Doherty, S., Harth, C., et al. (2019). Emissions of halocarbons from India inferred through atmospheric measurements. *Atmospheric Chemistry and Physics*, *19*(15), 9865–9885. https://doi.org/10.5194/acp-19-9865-2019

Simmonds, P. G., Manning, A. J., Cunnold, D. M., McCulloch, A., O'Doherty, S., Derwent, R. G., et al. (2006). Global trends, seasonal cycles, and European emissions of dichloromethane, trichloroethene, and tetrachloroethene from the AGAGE observations at Mace Head, Ireland, and Cape Grim, Tasmania. *Journal of Geophysical Research*, *111*(D18), D18304. https://doi.org/10.1029/2006JD007082

Simpson, I. J., Blake, N. J., Barletta, B., Diskin, G. S., Fuelberg, H. E., Gorham, K., et al. (2010). Characterization of trace gases measured over Alberta oil sands mining operations: 76 speciated C_2–C_{10} volatile organic compounds (VOCs), CO_2, CH_4, CO, NO, NO_2, NO_y, O_3 and SO_2. *Atmospheric Chemistry and Physics*, *10*(23), 11931–11954. https://doi.org/10.5194/acp-10-11931-2010

Simpson, I. J., Meinardi, S., Blake, N. J., Rowland, F. S., & Blake, D. R. (2004). Long-term decrease in the global atmospheric burden of tetrachloroethene (C_2Cl_4). *Geophysical Research Letters*, *31*(8), L08108. https://doi.org/10.1029/2003GL019351

Simpson, W. R., Brown, S. S., Saiz-Lopez, A., Thornton, J. A., & von Glasow, R. (2015). Tropospheric halogen chemistry: Sources, cycling, and impacts. *Chemistry Review*, *115*(10), 4035–4062. https://doi.org/10.1021/cr5006638

Sinnhuber, B. M., Sheode, N., Sinnhuber, M., Chipperfield, M. P., & Feng, W. (2009). The contribution of anthropogenic bromine emissions to past stratospheric ozone trends: A modelling study. *Atmospheric Chemistry and Physics*, *9*(8), 2863–2871. https://doi.org/10.5194/acp-9-2863-2009

Stephens, B. B., Long, M. C., Keeling, R. F., Kort, E. A., Sweeney, C., Apel, E. C., et al. (2018). The O_2/N_2 ratio and CO_2 airborne southern ocean study. *Bulletin of the American Meteorological Society*, *99*(2), 381–402. https://doi.org/10.1175/BAMS-D-16-0206.1

Stevenson, D. S., Zhao, A., Naik, V., O'Connor, F. M., Tilmes, S., Zeng, G., et al. (2020). Trends in global tropospheric hydroxyl radical and methane lifetime since 1850 from AerChemMIP. *Atmospheric Chemistry and Physics*, *20*(21), 12905–12920. https://doi.org/10.5194/acp-20-12905-2020

Sweeney, C., Karion, A., Wolter, S., Newberger, T., Guenther, D., Higgs, J. A., et al. (2015). Seasonal climatology of CO_2 across North America from aircraft measurements in the NOAA/ESRL global greenhouse gas reference network. *Journal of Geophysical Research: Atmospheres*, *120*(10), 5155–5190. https://doi.org/10.1002/2014JD022591

Thompson, C. R., Wofsy, S. C., Prather, M. J., Newman, P. A., Hanisco, T. F., Ryerson, T. B., et al. (2022). The NASA atmospheric tomography (ATom) mission: Imaging the chemistry of the global atmosphere. *Bulletin of the American Meteorological Society*, *103*(3), E761–E790. https://doi.org/10.1175/BAMS-D-20-0315.1

Tilmes, S., Lamarque, J. F., Emmons, L. K., Kinnison, D. E., Ma, P. L., Liu, X., et al. (2015). Description and evaluation of tropospheric chemistry and aerosols in the Community Earth System Model (CESM1.2). *Geoscientific Model Development*, *8*(5), 1395–1426. https://doi.org/10.5194/gmd-8-1395-2015

Tilmes, S., Lamarque, J. F., Emmons, L. K., Kinnison, D. E., Marsh, D., Garcia, R. R., et al. (2016). Representation of the Community Earth System Model (CESM1) CAM4-chem within the chemistry-climate model initiative (CCMI). *Geoscientific Model Development*, *9*(5), 1853–1890. https://doi.org/10.5194/gmd-9-1853-2016

USEPA. (2000). *Guidance for data quality assessment, practical methods for data analysis*. Office of Environmental Information Washington. EPA QA/G-9, QA00 Update Retrieved from https://www.epa.gov/sites/default/files/2015-06/documents/g9-final.pdf

van Herpen, M. M. J. W., Li, Q., Saiz-Lopez, A., Liisberg, J. B., Röckmann, T., Cuevas, C. A., et al. (2023). Photocatalytic chlorine atom production on mineral dust–sea spray aerosols over the North Atlantic. *Proceedings of the National Academy of Sciences of the United States of America*, *120*(31), e2303974120. https://doi.org/10.1073/pnas.2303974120

Wang, S., Apel, E. C., Schwantes, R. H., Bates, K. H., Jacob, D. J., Fischer, E. V., et al. (2020). Global atmospheric budget of acetone: Air-sea exchange and the contribution to hydroxyl radicals. *Journal of Geophysical Research: Atmospheres*, *125*(15), e2020JD032553. https://doi.org/10.1029/2020JD032553

Wang, S., Kinnison, D., Montzka, S. A., Apel, E. C., Hornbrook, R. S., Hills, A. J., et al. (2019). Ocean biogeochemistry control on the marine emissions of brominated very short-lived ozone-depleting substances: A machine-learning approach. *Journal of Geophysical Research: Atmospheres*, *124*(22), 12319–12339. https://doi.org/10.1029/2019JD031288

Wang, X., Jacob, D. J., Downs, W., Zhai, S., Zhu, L., Shah, V., et al. (2021). Global tropospheric halogen (Cl, Br, I) chemistry and its impact on oxidants. *Atmospheric Chemistry and Physics*, *21*(18), 13973–13996. https://doi.org/10.5194/acp-21-13973-2021

Wang, X., Jacob, D. J., Eastham, S. D., Sulprizio, M. P., Zhu, L., Chen, Q., et al. (2019). The role of chlorine in global tropospheric chemistry. *Atmospheric Chemistry and Physics*, *19*(6), 3981–4003. https://doi.org/10.5194/acp-19-3981-2019

Wiedinmyer, C., Kimura, Y., McDonald-Buller, E. C., Emmons, L. K., Buchholz, R. R., Tang, W., et al. (2023). The fire inventory from NCAR version 2.5: An updated global fire emissions model for climate and chemistry applications. *EGUsphere*, 1–45. https://doi.org/10.5194/egusphere-2023-124

Wiedmann, T. O., Guethner, B., Class, T. J., & Ballschmiter, K. (1994). Global distribution of tetrachloroethene in the troposphere: Measurements and modeling. *Environmental Science & Technology*, *28*(13), 2321–2329. https://doi.org/10.1021/es00062a016

Wofsy, S. C., Afshar, S., Allen, H. M., Apel, E. C., Asher, E. C., Barletta, B., et al. (2021). ATom: Merged atmospheric chemistry, trace gases, and aerosols, version 2. https://doi.org/10.3334/ORNLDAAC/1925

Worton, D. R., Sturges, W. T., Schwander, J., Mulvaney, R., Barnola, J. M., & Chappellaz, J. (2006). 20th century trends and budget implications of chloroform and related tri-and dihalomethanes inferred from firn air. *Atmospheric Chemistry and Physics*, *6*(10), 2847–2863. https://doi.org/10.5194/acp-6-2847-2006